GEOTECHNICAL ASSESSMENT OF UNITED STATES AND FOREIGN TEST SITES AND MATERIAL PROPERTIES OF GEOLOGIC MEDIA

Sponsored by:

Defense Advanced Research Projects Agency
ARPA Order No. 3134-A3

By:

H. R. Pratt	H. S. Swolfs
S. W. Butters	D. Gardiner

ARPA Order No. 3134-A3
Program Code No. 7F10
Program Element Code 62701E
Name of Contractor:
    Terra Tek, Inc.
Effective Date: Jan. 3, 1977

Amount of Contract: $78,583
Contract No. DNA 001-77-C-0122
Principal Investigator:
    Dr. Howard R. Pratt
    (801) 582-2220

The views and conclusions contained in this document
are those of the authors and should not be interpreted as
necessarily representing the official policies, either
expressed or implied, of the Defense Advanced Research
Projects Agency or the U.S. Government.

CLEARED
FOR OPEN PUBLICATION

'JAN 30 1985 19

DIRECTORATE FOR FREEDOM OF INFORMATION
AND SECURITY REVIEW (OASD-PA)
DEPARTMENT OF DEFENCE

REVIEW OF THIS MATERIAL DOES NOT IMPLY
DEPARTMENT OF DEFENSE INDORSEMENT OF
FACTUAL ACCURACY OR OPINION.

DTIC
SELECTED
FEB 22 1985
E

Terra Tek, Inc.
Salt Lake City, Utah
July, 1979
TR78-25

0 0343

ABSTRACT

This report presents a geotechnical assessment of geologic materials. This geotechnical assessment includes a compilation of both physical and mechanical property data for a wide variety of materials of interest to developing *in situ* constitutive relations for a variety of geologic environments. The data for shale, sandstone, granite and alluvium is presented. The *in situ* stress state was also defined for a variety of geologic and structural environments over a range of depths. An extensive experimental program was conducted on material from the GASSBUGGY site. These include data on the Picture Cliff sandstone and the Lewis shale. Triaxial tests including hydrostatic and uniaxial strain tests were conducted. Problems studied include the intact versus residual failure envelopes, the dilatent behavior of the shale and the sandstone and the dependency of modulus on strain-rate. These latter dynamic tests require the development of new experimental equipment.

Salt was also studied in detail. Cores from both the GNOME event and SALMON event were tested under triaxial conditions; both compression and extension failure envelopes were determined. The results indicate that the salt is ductile and shows no increase in strength beyond 0.7 kilobars stress difference for confining pressures up to 4 kilobars. The stress-strain response of a visco-elastic model was developed and used as the basis for analyzing the data from the dynamic tests conducted on the Lewis shale and Picture Cliff sandstone. The model is presented along with the dynamic data.

TABLE OF CONTENTS

1.0 INTRODUCTION

The objectives of the current program conducted for the Advanced
Research Projects Agency and the Defense Nuclear Agency were to evaluate,
analyze and develop material properties of geologic media for use in the
calculation of reduced displacement potentials and to conduct a geotech-
nical analysis of specified tests sites in both the United States and
foreign countries.

The geotechnical studies have included detailed analysis of sites in
the United State and foreign countries. The foreign sites have been
analyzed in cooperation with the U.S. Geological Survey, Reston, VA,
especially Jack Racklin and William Dempsey. These test sites have been
analyzed with respect to lithology and geologic structure. Material
properties for several foreign sites were estimated based on data from
analogous United States test sites. On the basis of all these data,
geologic models for the sites were formulated. These data were reported
in technical report entitled "Estimated Material Properties of U.S.S.R.
Test Sites" (Classified).

Analysis of the current state-of-the-art with respect to testing
rock in the Soviet Union was also investigated. Analysis of the U.S.S.R.
paper "Statistical Principals of the Strength and Deformation of the
Rocks in Complex States of Stress" by A.F. Stavrogin was reviewed to get
a current feeling of a state-of-the-art of rock mechanics in the Soviet
Union. In addition, a number of American scientists, who have been
recent visitors to the Soviet Union, were contacted. Some Soviet
scientists from the Russian Academy of Sciences visited Terra Tek on two
separate occasions to discuss rock mechanics testing. Their techniques
were discussed at that time. The appropriate ASTM standard test methods

1

were analyzed and discussed for possible use in the Threshold Test Ban Treaty (TTBT) and Peaceful Nuclear Explosion Treaty (PNET) negotiations with the Russians as standard procedures for determining both the tensile and compressive strengths of rock and for obtaining physical properties such as density, porosity, etc.

Dr. Pratt has also been participating in the working group of the ARPA seismic review panel and has discussed the verification and use of data to be exchanged under the Threshold Test Ban Treaty and Peaceful Nuclear Explosion Treaty. A number of meetings were held to delineate the packages to be exchanged between the United States and U.S.S.R. and to analyze the various potential test sites. The first section of the report includes a summary of physical and mechanical property data on geologic material of interest. Testing techniques, outlined in the first section of this report, are currently being used to obtain physical properties that will be exchanged during the Test Ban Treaty. These include density, porosity, and water content. Preliminary cross plots of physical and mechanical property data, density, porosity, water saturation and compressional and shear wave velocities are included. In addition, a section on the role of *in situ* stress and its potential effect on the seismic signal from a nuclear event is discussed. The relation between *in situ* stress magnitudes and depth, age and tectonic environment is evaluated.

Terra Tek has been conducting a program of material properties tests from the GASBUGGY site to supply input data and material models for use in the calculation of reduced displacement potentials by Dr. Robert Bjork and Dr. Robert Allen (PACTECH). Material property tests that have been

2

conducted include hydrostatic, uniaxial strain and standard triaxial tests on both the Lewis shale and Picture Cliffs sandstone. The tests were conducted at moisture contents simulating the *in situ* environment. In addition, several load path tests were conducted following the load paths indicated by the calculations from PACTECH.

Several problem areas were discussed with PACTECH and it was decided to conduct tests to address ourselves to these areas which significantly affect the results of the Reduced Displacement Potential Calculations. The problem areas include (1) initial versus residual failure envelopes, (2) dilatancy, and (3) strain rate effects on modulus. These tests will enable us to delineate the respective influences of the static and dynamic moduli during loading and unloading in the seismic frequency range. The test procedure loaded the specimen in a one millisecond rise time to a few bars by dropping a weight on to the specimen and analyzing the stress relaxation with time using a laser interferometer. The problem areas delineated above have been studied and data and analysis is presented.

2.0 GEOTECHNICAL ASSESSMENT OF GEOLOGIC MATERIALS

This summary provides some physical and mechanical properties of selected earth materials. It is anticipated that these data taken from published results of laboratory and selected field tests will provide a "data-base" for those developing constitutive equations of geologic materials, calculating the response of geologic materials to some loading, conducting experiments in earth media, or considering soil or rock/ structure interaction. The geologic materials selected include:

granite

sandstone

shale

alluvium.

These materials were selected because of the existing data base and because existing foreign sites are situated in these materials. In addition, tests on shale, sandstone and salt have been conducted under this contract and are presented in a later section.

The material property data include a description of the "physical" nature of each material and the "mechanical" response to a variety of load paths. The physical properties include some indication of the mineral compostion, the density, the porosity and the grain size. The mechanical properties include the general quasistatic-room temperature stress-strain response up to stresses of the order of 6-10 kilobars, with limited hydrostatic compression data. Some high strain-rate tests and ultrasonic test data are also included.

Rock and Soils Included:

"Granite"[*]

> Westerly granite (Rhode Island)
>
> Climax Stock granodiorite (Nevada Test Site)

Sandstone

> Kayenta formation (Mixed Company site, Colorado)
>
> Nugget formation (Utah)

Shale

> Pierre formation (Middle Gust site, Colorado)
>
> Pierre formation (South Dakota)
>
> Lance formation (El Paso Wagon Wheel site, Wyoming
>
> Nevada Test Site formation (Yacht site, Nevada Test Site, Nevada)

Alluvium

> Yucca flat alluvium (Yucca flat, Nevada Test Site, Nevada)

Westerly Granite

The Westerly Granite is a fine-grained igneous rock, grayish pink in color and composed of quartz, potassium feldspar and plagioclase feldspar, with minor amounts of biotite and hornblende. Grain size averages about .75 mm. Porosity is less than one percent and permeability is very low.

---

[*]Granite rock here includes a broader based group of rocks than the usual granite as defined by the geologist, based on mineralogy. The group would include granite, monzonite, granodiorite, and diorite whose minerology differ, but whose mechanical properties will probably be similar.

Climax Stock Granodiorite

This rock is medium-grained, grayish white, with grain size ranging between .5 to 5 mm. It is composed of quartz, potassium and plagioclase feldspar and micas. The rock has a typical interlocking igneous texture resulting from crystallization from a molten state. Both porosity and permeability of the intact rock is very low.

Nugget Formation

The Nugget Formation is a fine-grained, buff colored sandstone composed primarily of quartz, minor feldspar and hematite. The cement is secondary silica. Grain size ranges between .1 to 1.3 mm. Porosity is low for a sandstone, approximately 4 percent.

Kayenta Formation

Kayenta Formation is a fine to medium-grained porous sandstone, buff colored to almost white, and is composed of subangular to rounded grains of quartz, feldspar, rock fragments and calcite. The cement is pre-dominantly calcite. Minor opaques and micas are also present. Porosity ranges between 15 to 25 percent. Bedding thickness ranges from a few inches to several feet.

Pierre Formation - Middle Gust Test Site, Colorado

The Pierre Formation is a soft fine-grained, gray to black clay shale with stringers of gypsum and sand size material. The clay content is very high. Pyrite is sometimes found in the clay shale unit. Bedding thickness is highly variable.

Lance Formation

The Lance Formation is a shale to silty-shale, medium to gray to black in color with light gray stringers of coarser silt and sand sized material. The coarser grained stringers have the texture and composition of a fine-grained sandstone and indicate that the variation in lithologic character sometimes occurs only over a very few millimeters distance. These stringers permeate the shale at orientations running from sub-parallel to perpendicular with respect to the primary bedding which is oriented perpendicular to the core axis.

Yacht Site Shale

The Yacht Site shale is a Paleozoic fine-grained black shale having contorted bedding planes, which vary in orientation over small distances. Silt size grains of quartz were very common in several layers, also some fine-grained carbonate is present.

Pierre Formation - Shale

The shale is part of the Cretaceous Pierre Formation and is a grayish-black, fine-grained shale with a high clay content. Bedding is usually thin and the rock is sometimes very fissile.

Yucca-Flat Alluvium

The alluvium is a weakly cohesive, poorly sorted clastic material composed largely of quartz, feldspar, clay minerals and rock fragments. Some carbonate may be present. Grain size ranges from silt size particles to cobbles a few centimeters in diameter.

7

2.1 Physical Properties

The physical properties for the materials of interest are present in Table 1. Table 2 summarizes the testing techniques and accuracies for the physical property methods. Accuracy was obtained from calibration tests. Error was calculated using average Nevada Test Site tuff values: (ρ_g = 2.40 gm/cm^3, ρ_w = 1.8 gm/cm^3, ρ_d = 1.45 gm/cm^3, and w = 19%).

Moisture Content. The moisture content is determined by weighing a sample before and after oven drying with a resulting accuracy of 0.13% H_2O due to loss of water during crushing.

Bulk Density. Dry or "as-received" bulk densities may be found from the volumes determined using (1) calipers, (2) the Ruska Mercury Porometer or (3) the water immersion method. If a precision machined sample is not available for caliper measurement, then for samples 30 cm^3 or larger, the Ruska Mercury Porometer should be used, whereas the water immersion method is better for volumes less than 30 cm^3.

Grain Density. The National Bureau of Standards powered silicon (SRM 640) and the crystalline quartz tests indicate that the Beckman Gas Pycnometer technique is more accurate and precise than the water immersion method (0.001 gm/cm^3 as compared to 0.010 gm/cm^3 respectively). Materials containing zeolites may lead to volume drift in the gas pycnometer unless the sample is allowed to equilibriate with atmospheric moisture prior to testing.

Total Porosity. The total porosity is calculated from the grain and dry bulk density values and consequently depends upon the techniques used

TABLE 1: PHYSICAL PROPERTIES

Name	Rock Type	Composition (Model %)	Grain Size (mm)	Density Bulk (gm/cc)	Density Grain (gm/cc)	Porosity (%)	Moisture Content Wt. %	Source
Westerly	Granite	28 Q, 35 K, 31 P, 5 M	0.75	2.646	2.65	~.9	Lab dry	Bonner Monument quarry Westerly R.I.
Climax Stock	Granodiorite	29 Q, 16 K, 45 P, 9 M (19 modes)	0.5-4.0	2.67-2.69	2.67-2.70	<1.0	Dry Saturated	Climax Stock Area 15 Nevada Test Site, Nye Co., Nev.
Nugget Fm.	Sandstone	96 Q, 2 K, 2 Op	.07-0.3	2.52	2.625	4.0	Dry	Perley's Canyon, Salt Lake Co., Utah
Kayenta Fm.	Sandstone	70 Q, 10 P, 8 Cc, 8 RF, 2 M	.1-.4	1.91-2.20 1.967-2.01 2.08	2.65	14-20 20.4 21.2	Dry	Mixed Company test site Mesa Co., Colorado
Pierre Fm.	Shale	Cm, Cc, Q	<.05	2.07	2.71	8.0	As received Saturated	Middle Gust test site, Ordway, Colorado
Lance Fm.	Shale	33 Q, 34 Cm, 13 Cc, 16 RF, 2 M	.03-0.2	2.47	2.65	8.0	Dry	El Paso Natural Gas Co. Wagon Wheel Well No. 1, Depth 10215, Sublette Co. Wyoming
Yacht	Shale	10 Q, 80 Cm, 3 Cc, 7 Op	<0.03	2.64	2.75	4.0	Dry	Hole UE11, Nevada Test Site, Nye Co., Nev.
Pierre Fm.	Shale	Q, Cm, Op	<0.03	2.11	2.70	22.0	As received (mom. sat'd)	U2 Minuteman Site
Yucca Flat	Alluvium	Variable	.1-30	1.57			Dry, 7, 10, 17	Area 3 hole tel-ct, Nevada Test Site, Nye Co., Nev.

* Q = Quartz P = Plagioclase feldspar Cc = Calcite RF = Rock fragments

K = Potassium feldspar M = Mica Cm = Clay minerals Op = Opaques

9

Table 2

Accuracy and Error of Physical Property Methods

PHYSICAL PROPERTY	HOW DETERMINED	ACCURACY*	STRUCTURAL INTEGRITY ROCK NECESSARY FOR MEASUREMENT
Moisture Content (w)	Weight determined using electronic balance	0.13% w	poor to good
Wet Bulk Density (ρ_w)	Volume measured using 1) Calipers 2) Ruska Mercury Porometer 3) Water Immersion	1) -.014 to -.028 gm/cc 2) .001 gm/cc ±.002 gm/cc 3) -.002 gm/cc ±.004 gm/cc	1) fair to good 2) fair to good 3) poor to good
Dry Bulk Density[†] (ρ_d)	1) Calc. using w and ρ_w 2) Calipers 3) Ruska Mercury Porometer 4) Water Immersion	1) .004 gm/cc ± .002 gm/cc 2) -.017 to -.031 gm/cc 3) .004 gm/cc ± .002 gm/cc 4) .001 gm/cc ± .004 gm/cc	1) refer to w & ρ_w 2) fair to good 3) fair to good 4) poor to good
Grain Density (ρ_g)	Volume measured using 1) Water Immersion 2) Gas Pycnometer	1) .01 gm/cc ± .04 gm/cc 2) .001 gm/cc ± .005 gm/cc	1) poor to good 2) poor to good
Total Porosity** (n_t)	Calculated from ρ_g and ρ_d	-0.14%n_t ± .21%n_t	fair to good
Effective Porosity (n_e)	1) Ruska Mercury Porometer 2) Water Immersion 3) Gas Pycnometer	0.53% n_e	1) fair to good 2) poor to good 3) poor to good
Permeability (K)	Permeability equipment	Repeatable to within 20%	poor to good
Air Voids** (Av)	Calculated from ρ_g, ρ_d, ρ_w	.16% Av ± .44% Av	refer to densities
Saturation** (Sr)	Calculated from w, n_t, ρ_w	0.26% Sr ± .56% Sr	refer to e, n_t, ρ_w
Microscopic Analysis (Grain size, orientation and mineral content	1) Large grain method using Bausch and Lomb Monocular 2) Medium grain method using Zeiss 3) Medium grain method using universal stage 4) Small grain method using scanning electron microscope	For all microscopic methods accuracy is dependent upon magnification level and smallest grain size	1) poor to good 2) fair to good 3) fair to good 4) poor to good

* Errors may be calculated using average NTS tuff values (ρ_g = 2.40 gm/cm^3. ρ_w = 2.80 gm/cm^3, ρ_d = 1.45 gm/cm^3, and w = 19%)

** Accuracy calculated from Ruska Porometer and Beckman Pycnometer values.

† Dry Bulk density accuracy includes moisture content error.

in those determinations. Using the most accurate techniques, the total porosity accuracy is within -0.35 percent n_t to 0.07 percent n_t.

Effective Porosity. Effective porosity is determined using water immersion, mercury injection (Ruska Mercury Porometer) and gas pressurization (Beckman Gas Pycnometer). The Ruska Mercury Porometer required knowledge of the mean sample pore size for complete effective volume determination. While the gas pycnometer can determine effective pore volume, it cannot easily measure bulk volumes, thus, requiring another method to determine sample bulk volumes. Only the water immersion method is self-contained in that both bulk volume and effective pore volume may be determined using the same piece of equipment. No effective porosity standard exists, but method comparison showed the effective porosity to be repeatable to within 0.53 percent n_e.

Percent Saturation and Percent Air Voids. Enumeration of these properties is subject to accumulated error from density, porosity and percent mositure determinations. The accumulated accuracies for each property are shown in Table 2. The percent saturation and percent air void accuracies are computed using the most accurate techniques for density, porosity and percent water.

Permeability. Permeability may be determined by either a transient or a steady-state method. No generally accepted permeability standards are available, but comparisons and variations in method suggest the values are repeatable to within 20%.

11

Microscopic Analysis. Microscopic analysis consists of grain size, spatial orientation and mineral content determination. Four methods are available, each of which has its advantages. Mineral content analysis is not possible using the scanning electron microscope (Method IV). However, it provides means of testing low cohesion rock fabrics as does the "large grain method" (Method 1). The "medium grain techniques" (Methods II and III) require fair to good cohesive rock fabrics because of thin-sectioning and handling. As stated in Table 2, the determining factors deciding which method to use are the grain size and the structural integrity of the rock.

In order to provide a "feeling" for the relationship between various parameters to physical properties cross plots relating porosity, density, velocity and modulus are given in Figures 1 - 4.
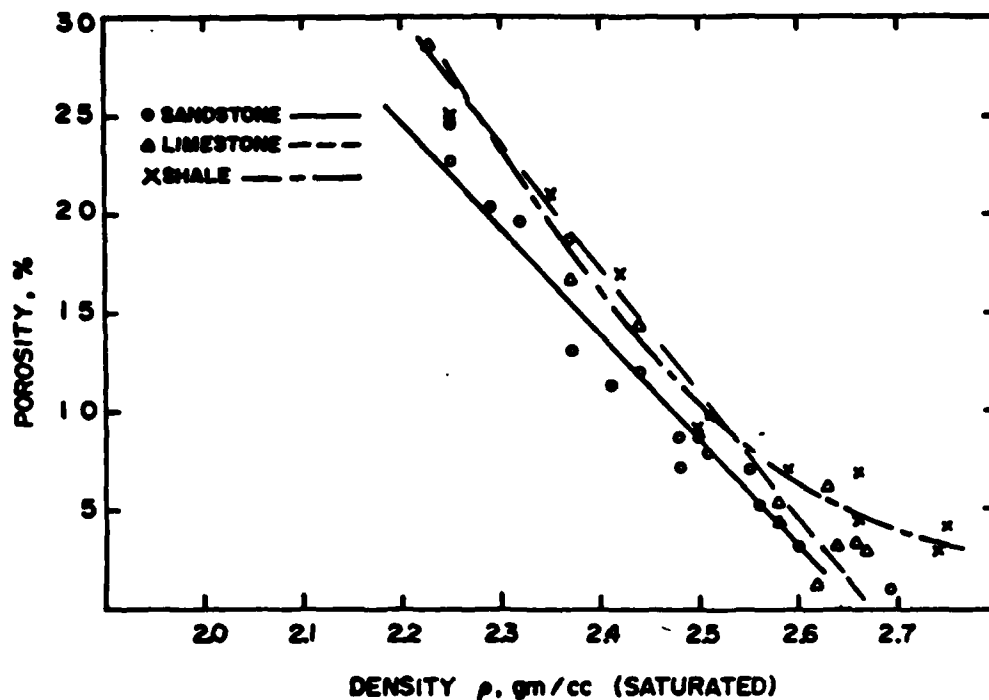
Figure 1. Density vs. porosity (field and lab) -
sedimentary rock.
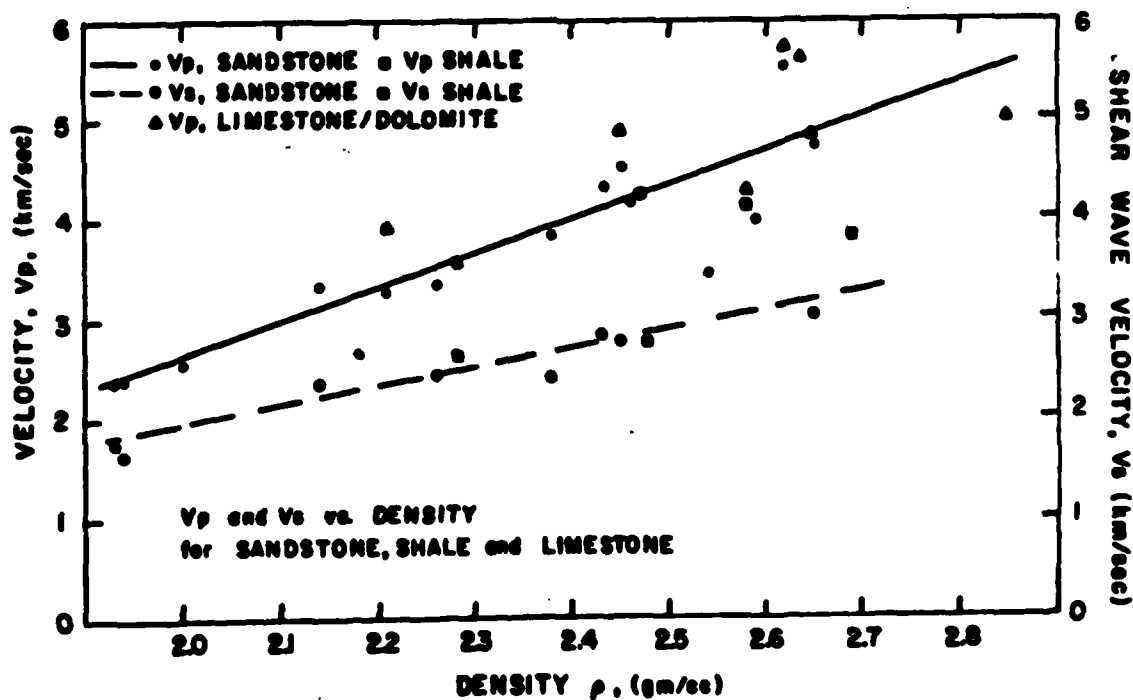
Figure 2. Density vs. V_p and V_s (field and lab) -
sedimentary rock.

13
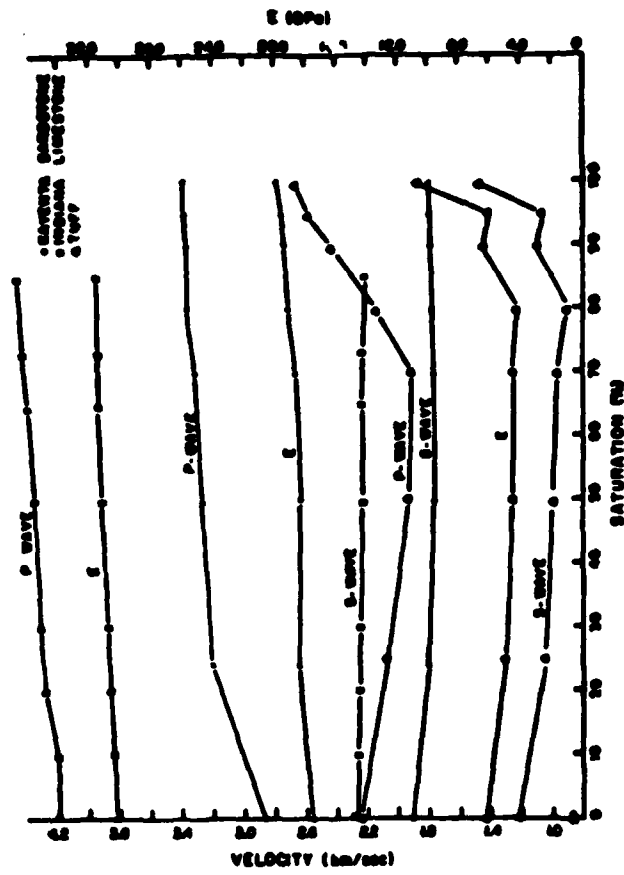
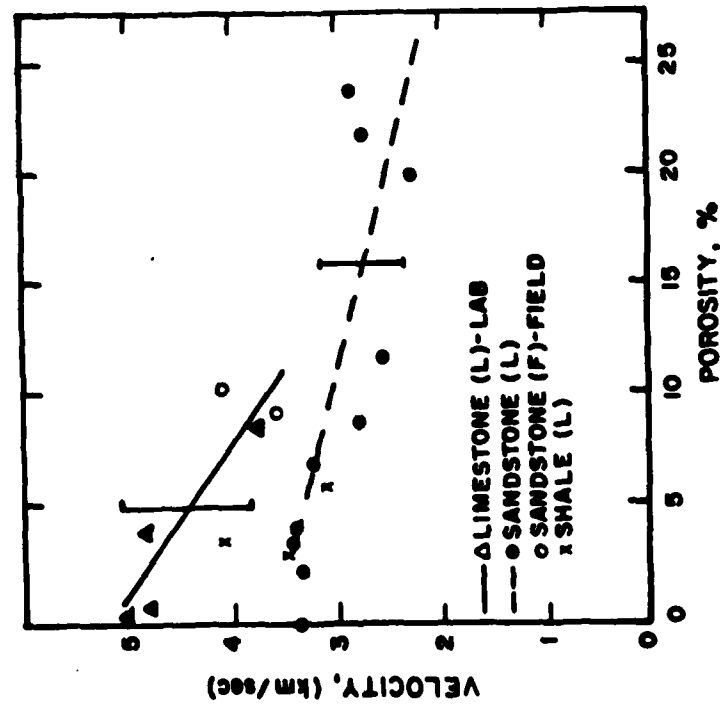Figure 4. V_p, V_s, and modulus (E) vs. saturation

Figure 3. Porosity vs. V_p (lab) - sedimentary rock.

△ LIMESTONE (L)-LAB
● SANDSTONE (L)
○ SANDSTONE (F)-FIELD
× SHALE (L)

POROSITY, %

VELOCITY, (km/sec)

SATURATION (%)

VELOCITY (km/sec)

E (GPa)

14

2.2 Mechanical Properties

Laboratory tests have been conducted on geologic materials for some
time, however, these tests have to a large extent been restricted to uncon-
fined and triaxial stress tests to high pressure on strong rocks[2,3] and to
constrained tests on soils at low stresses[4]. The development of servo-
controlled machines for testing rock in the late 1960's[5] allowed a variety
of load path tests to be conducted ranging from uniaxial strain to propor-
tional loading at stress levels exceeding several kilobars (Table 3). Pore
pressure measuring devices are also now capable of applying pressures up to
several kilobars. Other static loading apparatus using piston cylinder
dies employing a solid pressure transmitting media has been used to static
pressure of 40 kilobars[6]. Loads could generally be adequately determined,
and strain gages attached to the surface--or to thin metal jackets contain-
ing the rock provided strain measurement. Laboratory sample sizes usually
ranged from 2.5 to 10.0 cm in length with a characteristic $L/D = 2.0$. Large
loading frames and pressure vessels now allow testing on samples up to 30.0
cm in length to confining pressures of 2.0 kilobars.

Special techniques were required to load and to measure strains for
less competent geologic materials such as tuffs, shales, soils, alluvium.
Mechanical extensometers were developed in the early 1970's[7] for adequately
measuring large strains. Specimen preparation, and particularly sealing
the specimen from confining-fluid intrusion required special development
in order to conduct tests to multikilobar stress levels. Sealing can now
generally be accomplished for a variety of materials.[8] Strain rate effects
have been studied over a wide range of loading rates from 10^{-5} to 10^{-1},
using static testing equipment[9] and $10^3/sec^{-1}$ using shock loading
techniques[10,11].

15

To obtain material properties in the 10 to 40 kilobar range, solid media apparatus have been developed to measure the pressure-volume response. At pressures exceeding approximately 40 kilobars, one dimensional shock wave experiments are used to provide most of the information on material properties. These experiments measure either stress or particle velocity in the direction of a propagating wave in the shock front.

Techniques have been developed to measure the frictional properties of jointed material including strength, coefficient of friction and "stiffness" under a variety of loading conditions[13-16]. The various types of shear tests include triaxial, direct and torsional shear tests. Experiments have been conducted with a variety of controlled conditions along the joint or fracture including a variety of surface roughness, pore pressures and joint orientations[17-18].

The data from the laboratory tests are plotted in terms of the principal stress σ_1, σ_2 and σ_3 for the various tests listed in the table below.

TABLE 3

EXPERIMENTAL CONDITIONS

Test Method	Stress State	Properties Measured
Uniaxial loading	$\sigma_1 > 0; \sigma_1 < 0$ *	Stress-strain behavior; ductility "yield" strength; ultimate stress under static and cyclic loading; effects of temperature and strain rate deformation and fracture mechanisms.
Triaxial compression	$\sigma_1 > \sigma_2 = \sigma_3$	Same as above; pore pressure effects, friction on joints
Triaxial extension	$\sigma_1 = \sigma_2 > \sigma_3$	Same as above
Uniaxial strain	$\varepsilon_1 > 0$ $\varepsilon_2 = \varepsilon_3 = 0$	Same as above
Direct shear Triaxial shear	Multiaxial	Shear strength on prescribed planes including joints; pore pressure effect; friction on joints

* $\sigma_1 > 0$ denotes compression
$\sigma_1 < 0$ denotes tension

16

The data for each rock type is presented as a series of plots covering the stress range of interest.

Figures 5 - 9 give the plots available for each rock type covering the range of stress states and strain rates of interest. Average or best curves have been selected for those curves studied by several investigators. The summary plots include:

        (1) Hydrostats (Figure 5)

        (2) Stress-strain (Figure 6)

        (3) Failure envelopes   (Figure 7)

        (4), Uniaxial strain   (Figure 8)

        (5) Seismic velocity vs. σ (Figure 9)

These composite plots are presented so that comparisons between various materials can be made.

In addition to mechanical property data, sonic velocity data are presented when available. The apparent elastic moduli can be scaled from the tangents to slopes of the stress-strain curves, and the apparent bulk moduli can be scaled from the mean normal pressures, P_m vs. axial strain curve under hydrostatic loading where:

$$P_m = 1/3 \ (\sigma_1 + \sigma_2 + \sigma_3).$$

In the deviatoric plane, the square root of the invariants of stress and strain are defined in terms of the principal stresses and strains as:

$$\sqrt{J_2'} = (1/\sqrt{6}) \ \sqrt{(\sigma_1-\sigma_2)^2 + (\sigma_2-\sigma_3)^2 + (\sigma_1-\sigma_3)^2}$$

$$\sqrt{T_2'} = (1/\sqrt{6}) \ \sqrt{(\epsilon_1-\epsilon_2)^2 + (\epsilon_2-\epsilon_3)^2 + (\epsilon_1-\epsilon_3)^2}$$

The relationship between the shear stress and strain, τ and γ, in triaxial tests and the invariants $\sqrt{J_2'}$ and $\sqrt{T_2'}$ are:
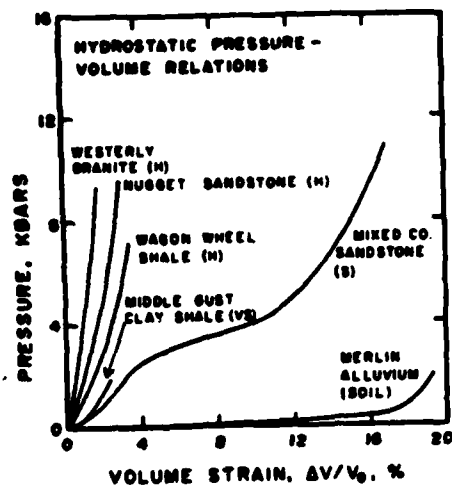
17

Figure 5. Hydrostatic Pressure - Volume Response
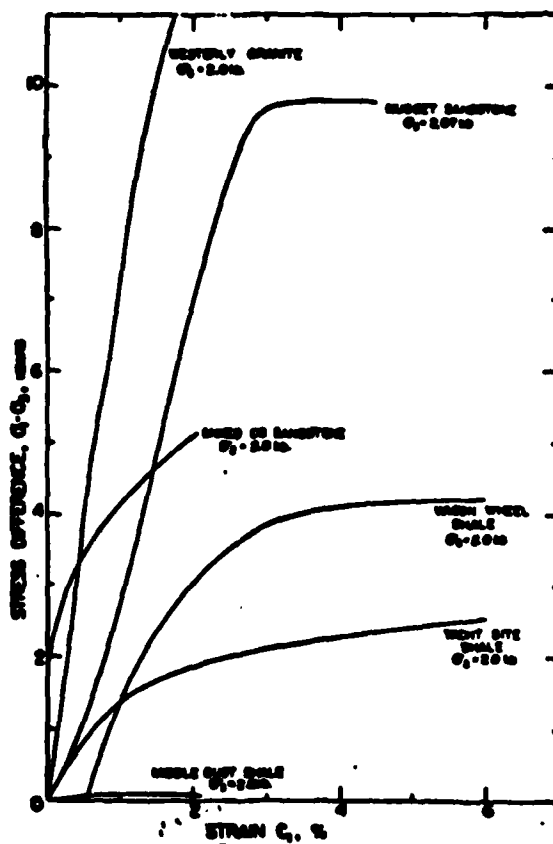of several rocks and alluvium.

Figure 6. Stress difference as a function of axial
strain for shale, sandstone and granite
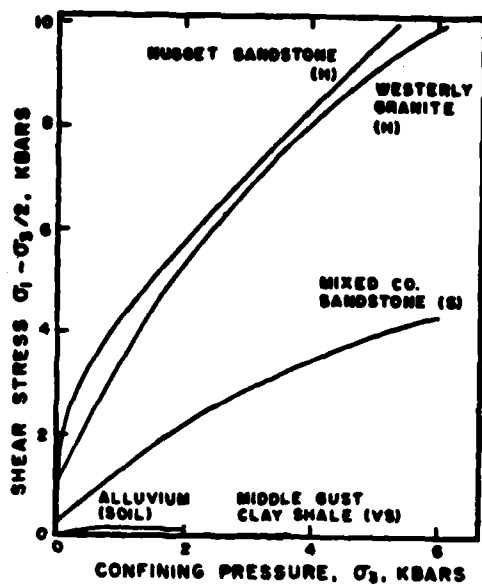at 2 kilobars confining pressure.

18

Figure 7. Comparison of the failure envelopes for
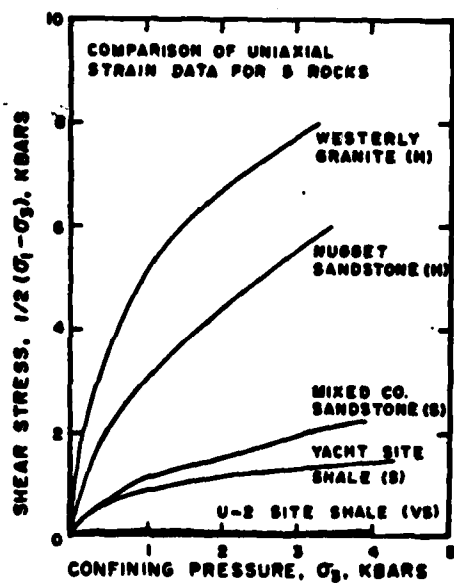shale, sandstone, granite and alluvium.

Figure 8. Comparison of the uniaxial strain response
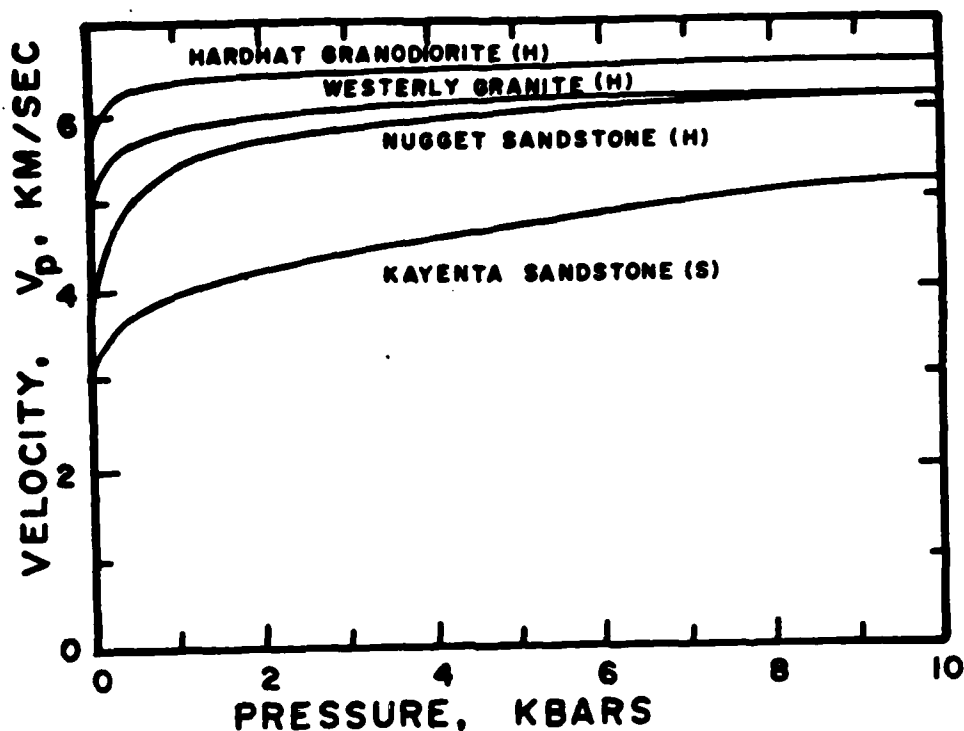for shale, sandstone and granite.

Figure 9. Velocity as a function of pressure for a
variety of rocks.

$$\sqrt{J_2'} = (2/\sqrt{3})\tau$$

$$\sqrt{T_2'} = (1/\sqrt{3})\gamma$$

The apparent shear moduli are scaled from the slope of the shear stress-
strain curves.

In addition to the coefficient of friction, the frictional properties
determined from triaxial or direct shear tests most commonly used in cal-
culations are the shear and normal stiffness. These parameters are scaled
from the shear stress-shear displacement and normal stress-normal displace-
ment curves, respectively (Figures 10 and 11)[19,18]. The roughness of the
discontinuity, type gouge, filling material, effect of water and load path
all have pronounced effects on frictional strength.

20

The effect the degree of saturation is also shown for a number of the rocks and soil where data is available (Figure 12)[20]. In addition, the effect of fracturing and pore pressure on the strength of hard granodiorite is given[21]. Note the magnitude of the decrease in strength between intact and fractured rock and the role of pore pressure to decrease strength (Figure 13). The role of moisture content on failure strength of granite is also given (Figure 14)[22]. Note the total lack of increased strength with confining pressure with excess water available. Mechanical property data from these rocks as well as Nevada Test Site data on tuff are summarized in Table 4.
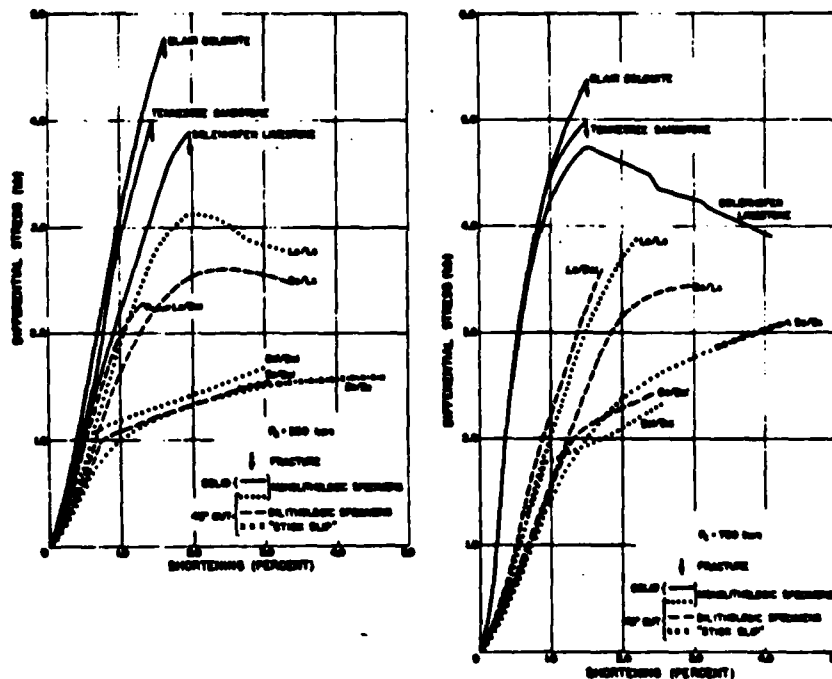
Figure 10. Differential stress vs. axial shortening curves at three different confining pressures for intact specimens (solid curves), monolithologic saw-cut specimens (dotted curves), and dilithologic specimens (dashed curves). Curves are averages of two or more experiments.[19]
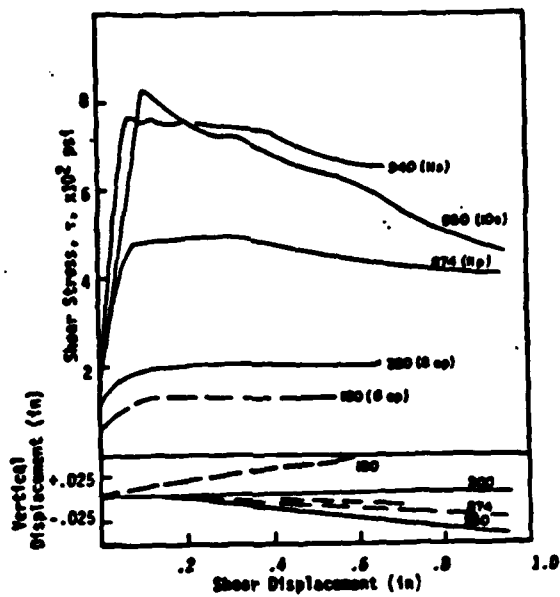
Figure 11. Shear stress vs. displacement curves for shear tests at a variety of normal stresses. From this curve the frictional failure envelope and the shear stiffnesses can be determined.[16]
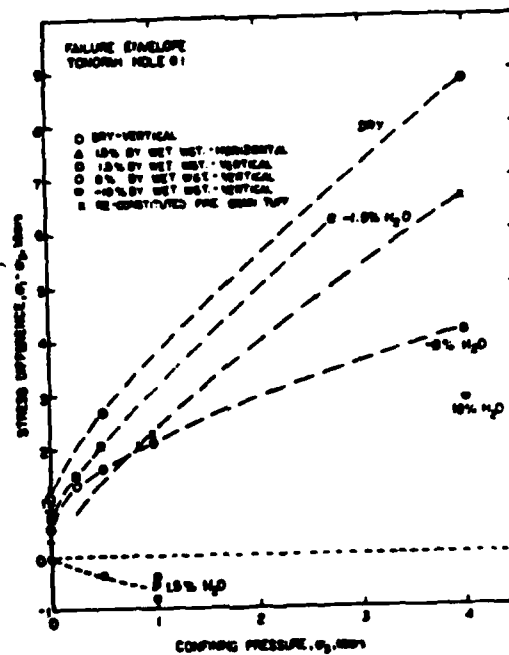

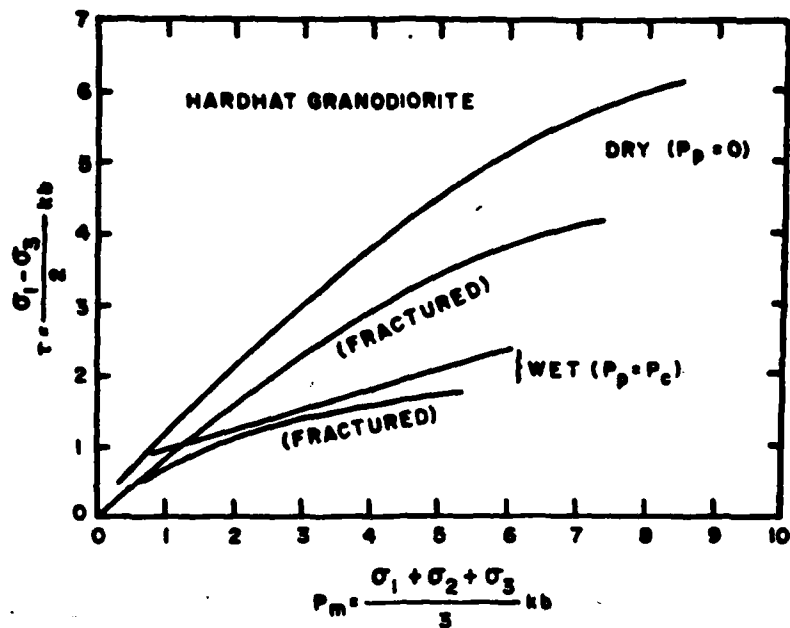Figure 12. The failure envelope of welded tuff from the Central Nevada Test Site as a function of water content [20].

22

Figure 13. Failure envelopes above intact and fractured
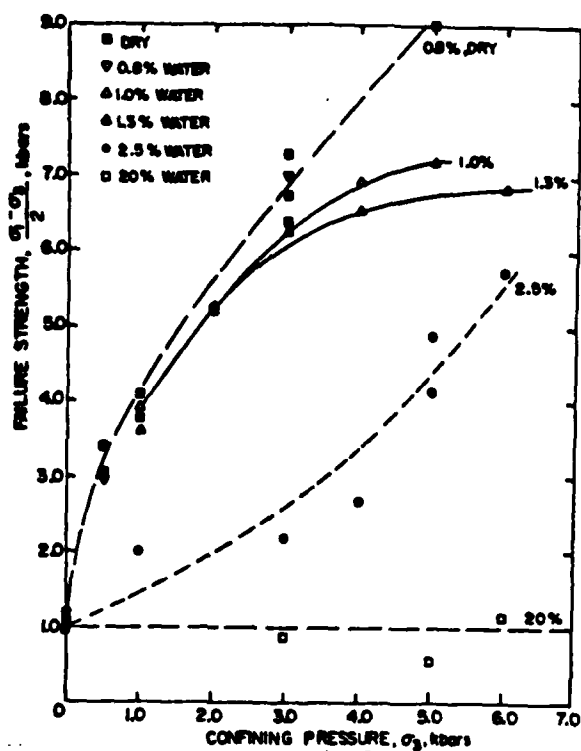Climax Stock granodiorite under dry and
saturated conditions [21].

Figure 14. Failure strength of Westerly Granite as a
function of confining pressure for dry samples
and samples with a variety of water contents[22].

23

TABLE 4

ROCK TYPE (Formation)	UNCONFINED STRENGTH (kb)	TENSILE STRENGTH	STRENGTH DIFF. (kb)	SHEAR MODULUS (kb)
Igneous				
"Volcanic"				
Tuff				
Ranier Mesa	0.06 - 0.10	0.01	0.35 - 0.65	4 - 13
Pahute Mesa (more welded)	0.50 - 0.65	0.035		40.0-55.0
"Granitic"				
NTS Granodiorite	1.8			271
Westerly	2.4	.113		227
Sedimentary				
"Sandstone"				
Nugget	2.0	.117		140
Lance (Wagon Wheel)	1.5	.054	14.5	125
Picture Cliff (Gassbuggy)				
"Shale"				
Lance (Wagon Wheel)	1.16		8.0	118
"Limestone"				
Solenhofn	2.8		6.0	262

For the purposes of comparison the published[23] geology (rock type) of Soviet test sites is given in Table 5 as well as the number of events.

TABLE 5

SOVIET PNE SITES	
Rock Type	**No. of Projects**
Shale/Sandstone	4
Sandstone	9
Limestone & Dolomite	8
Gypsum	1
Salt	3
Granite	7

2.3 *In Situ* Stress Environment

The role of *in situ* stress on the development of constitutive models for geologic materials is quite evident from nuclear events. *In Situ* tectonic stress can grossly affect the seismic radiation pattern (Figure 15). Seismic radiation is antisotropic and thought to be the result of the release of tectonic stress during the PILE DRIVER and GREELEY events [24]. The exact contribution of the tectonic stress is not known at this time. In order to better understand the role of *in situ* stress we have plotted the *minimum horizontal* stress versus the vertical stress as a function of depth for a variety of materials (Figure 16). As one can see, in the near-surface environment where NUCLEAR EVENTS are usually conducted, the ratio of the stresses can range from 0.4 to 3, depending on the rock type. Recent data has indicated that more ductile materials such as shales show a minimum to vertical stress on the order of .8 to 1 regardless of depth up to a few kilometers.

Hydraulic fracturing data in crystalline rock and indicates that the stress state varies depending on the tectonic environment (Figure 17). The plot shows environments for normal (N), strike slip (S) and thrust (T) fault areas. The data correlates well with the actual geologic structure in the area. This may enable us to take a first cut of evaluating the stress state for a particular geologic area based on reconnaissance field data. Figure 18 shows the plot of a square root of $\sqrt{J_2'}$ (shear stress invarient) as a function of mean pressure. This data indicates that significant deviatoric stresses occur in *in situ* crystalline rock and indeed indicates that granites may be under a tectonic stress environment relatively near the failure envelope. Their data would be exemplified by the *in situ* stress data from the Rocky Mountain Arsenal, where it only took a few
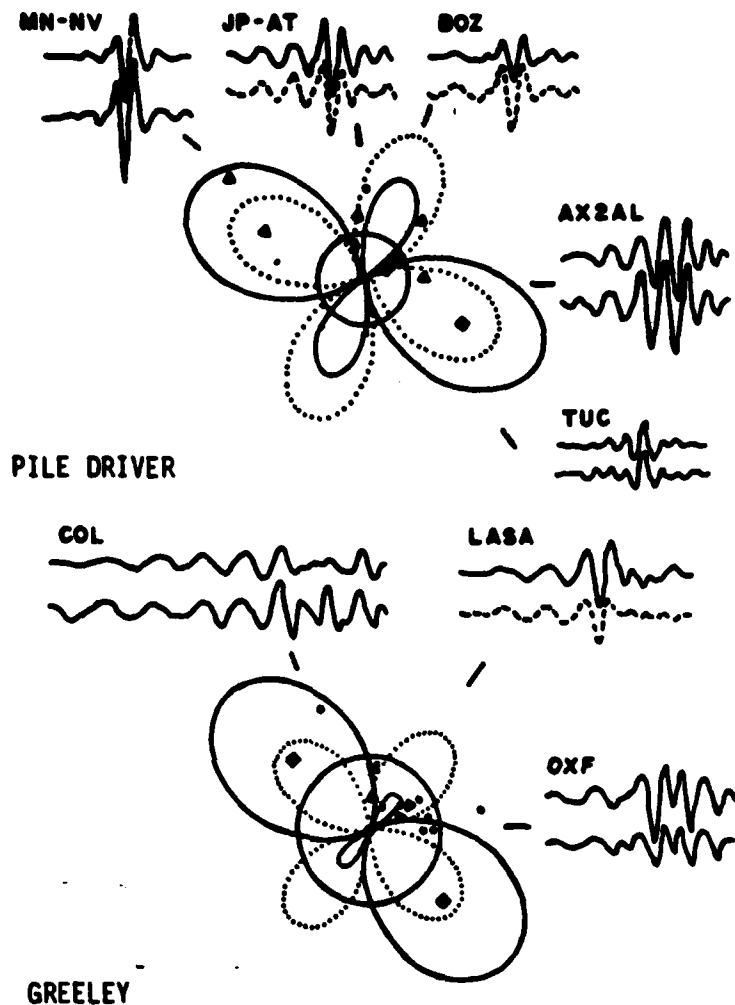
25

Figure 15. Raleigh wave seismic radiation patterns from events PILE DRIVER and GREELEY showing the anistropic nature of the radiation. The explosive source (solid circles), strain release component (dashed curves), and composite sources representing theoretical models (solid curves) are shown from various stations (MN-NV, JP-AT, BOZ, AXZAL, TVC, COL, LASA, OXF).[24]
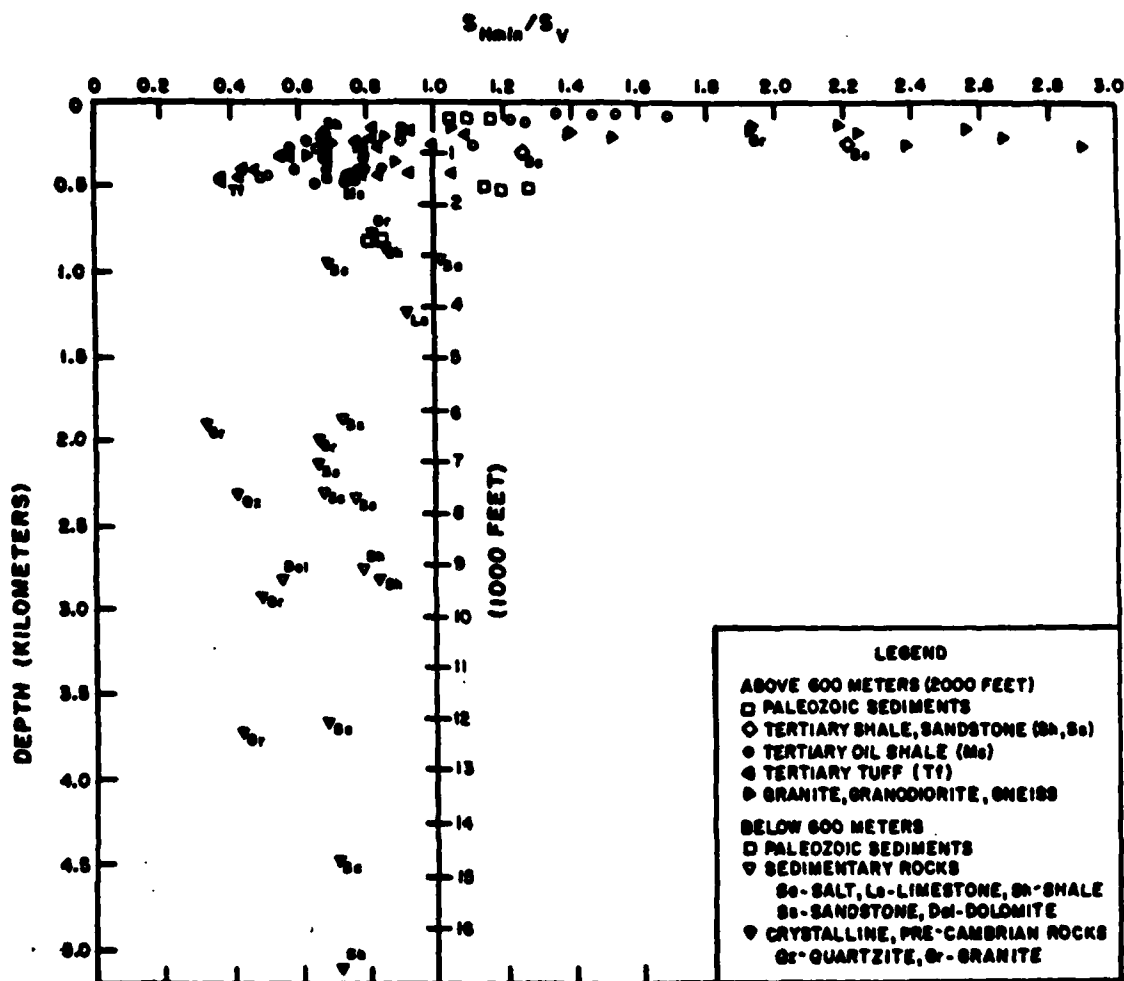
Figure 16. The ratio of the horizontal minimum stress
to vertical stress as a function of depth for
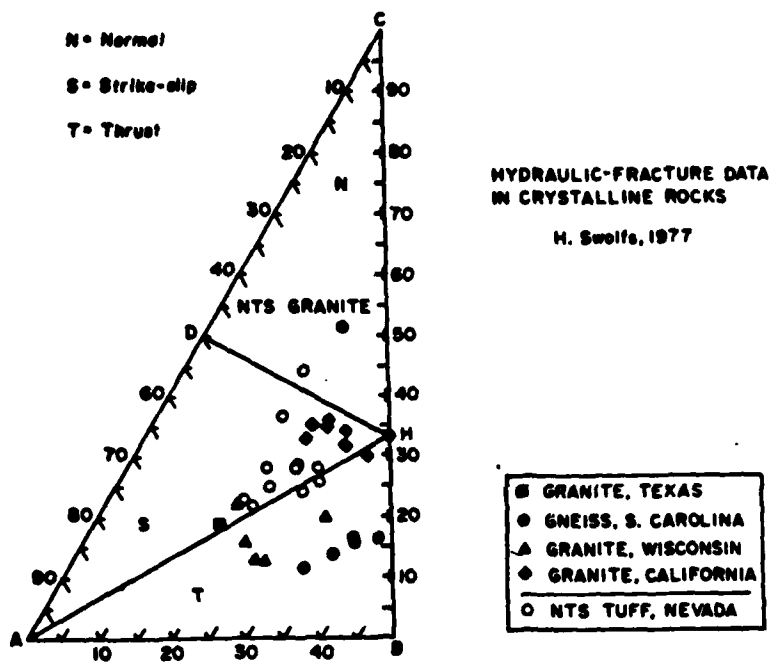a wide variety of geologic materials.

27

Figure 17. Hydraulic fracturing data in Crystalline rock
showing the relationship of the measurements to known tectonic
environments. Point H represents hydrostatic loading where
$\sigma_1 = \sigma_2 = \sigma_3$. N, S and T represent normal, strike-slip and
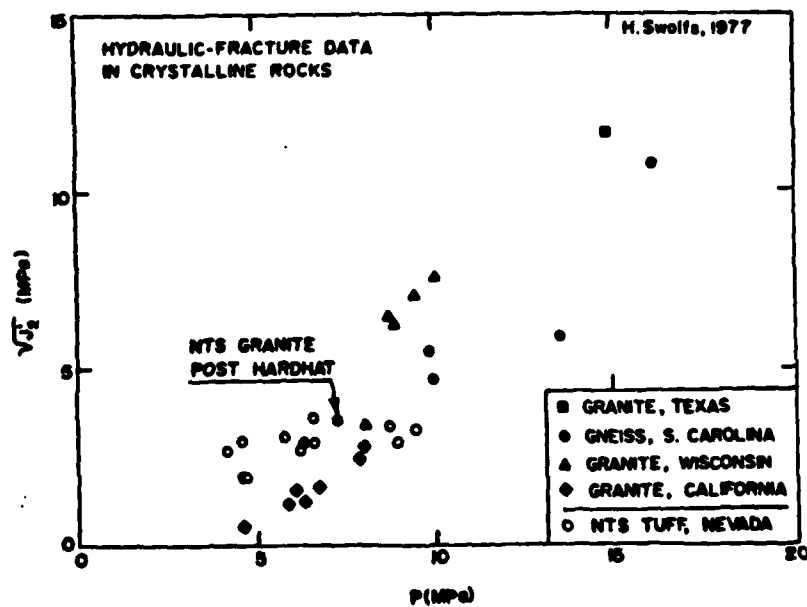thrust faulted regions. Corners C and A of the diagram represent
σ_1 and σ_3, respectively.

Figure 18. Hydraulic fracture data in crystalline rock.
Shear stress invarient vs. mean pressure indicating that these
rocks are not under hydrostatic stress _in situ_.

28

bars of increased pore pressure to cause the rock to fail (earthquakes).
This data has implications of the potential for tectonic stress relief
and for "block motion" displacements associated with nuclear events[25,26].
The equation for horizontal stresses in a near surface region and at depth
has been derived (Figure 19) these data will allow us to reasonably pre-
dict the stresses for a given geologic environment. It must be emphasized
that the "Tectonic environment" must be evaluated in order to assess the
relevance of the data. The relationship of stress to age has been compiled
in Figure 20 where the ratio of the horizontal minimum stress to the vertical
stress is plotted as a function of depth for three groups of rock: granites,
gneiss and tuffaceous rock. Note that the younger rocks have a lower stress
ratio than the older materials. We may be able to develop a correlation
between age and stress ratio, which may enable us to draw conclusions about
the *in situ* stress state at various sites based on geotechnical data.

In summary, several conclusions can be drawn: (1) the natural *in situ*
stress state is not hydrostatic (2) crystalline rocks show a wide variety
of stress ratios while rocks such as salt and shale are nearly under a
hydrostatic stress state (3) the existing tectonic environment influences
the *in situ* stress state (4) the depth of implacement of crystalline rock
may be important to the *in situ* stress field (5) the *in situ* stress state
does have an effect on the seismic radiation pattern and may be a source
of energy for "block motion" displacements in fractured rock (6) based on
the available data there seems to be a relationship between stress ratio
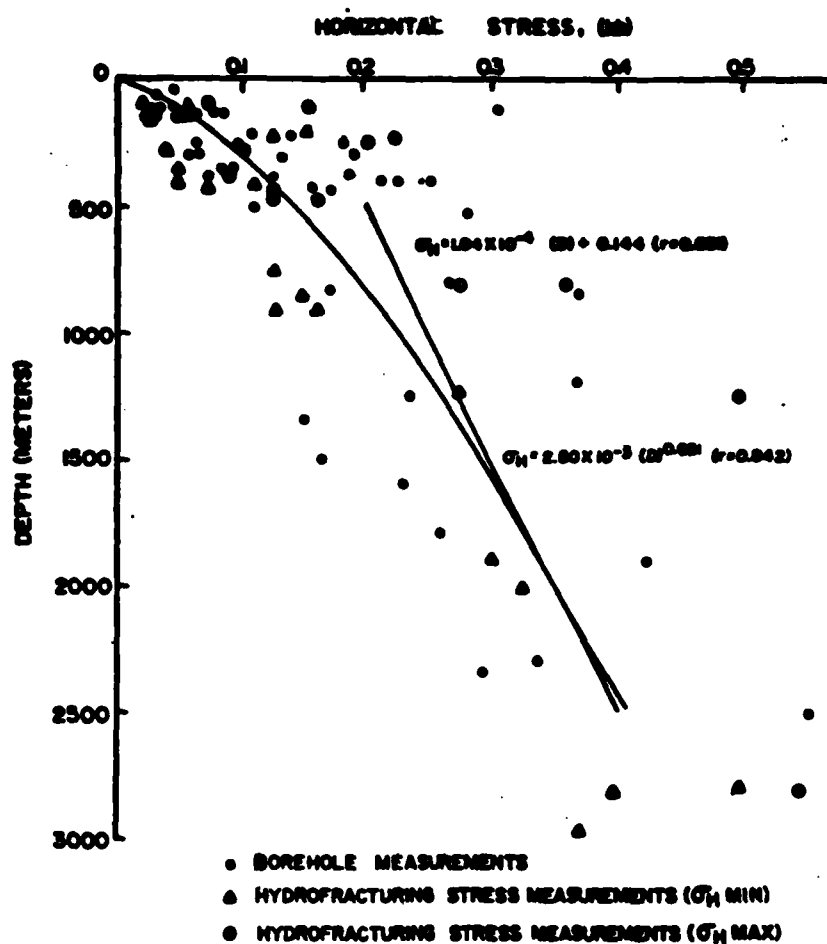and age of the rock mass.

Figure 19. Horizontal stress vs. depth for a variety of
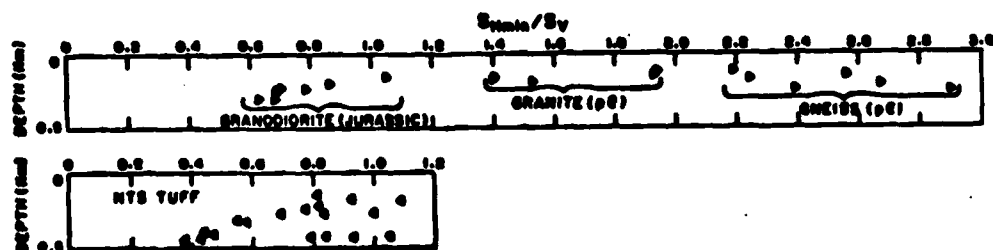stress measurement techniques.

Figure 20. Horizontal minimum/vertical stress ratio as a function of
depth for rocks of different ages. Crystalline rocks and
tuffaceous rocks are plotted.

30

3.0 MATERIAL PROPERTY TESTS

3.1 Introduction

This section presents the results of a series of material property tests conducted on a variety of rock types in the support of a calculational program to obtain the reduced displacement potential for a variety of rock types. The properties measured include grain density, bulk density, porosity and degree of saturation. Several kinds of laboratory tests were conducted on three types of rock--sandstone, shale and salt. The tests included uniaxial compression and triaxial tests under a variety of load states. These triaxial load paths include hydrostatic, uniaxial strain, extension and a series of tests conducted to simulate the loads followed during a calculation of the GASSBUGGY site response conducted by PACTECH. In addition, the material properties of a bedded and domal salts were compiled and determined the range of expected physical and mechanical properties.

The GASSBUGGY materials, the Picture Cliffs sandstone and the Lewis shale were chosen because the nuclear event provided some of the best data points for the measurement of reduced displacement potential, and therefore, provided a basis from which the numerical modeling people could determine how well they could calculate the reduced displacement potentials given the laboratory material properties.

3.2 Experimental Procedures

The experimental procedures used for obtaining various physical and mechanical properties are outlined briefly below. (More detailed discussion of experimental procedures, especially for the triaxal test conditions is given in Butters, et al.)[29]

31

3.3 GASSBUGGY Event Material Response

The physical and mechanical properties of the two rock types of
interest from the GASSBUGGY site, the Picture Cliffs sandstone and the
Lewis shale were tested and analyzed in detail. The GASSBUGGY test was
a 28 kiloton nuclear event to determine the feasibility of nuclear
stimulation of a gas field. The event was detonated in the Lewis shale
and had depth of approximately 4,200 feet, approximately 40 feet below
the interface between the Lewis shale and the overlying Picture Cliffs sand-
stone so that both properties of the shale and the sandstone dictate the
response of the rock mass of interest (Figure 21)[26]. A summary of the
physical and mechanical properties of the Picture Cliffs sandstone and
the Lewis shale are given in Table 6. This is a compilation from both the
tests Terra Tek conducted in this program and from other sources.

The response of the Lewis shale to various triaxial loading conditions
including compression, uniaxial strain and hydrostatic loading conditions is
given in Figures 22-25. Figures 26 through 28 show the same set of tests for
the Picture Cliffs sandstone. The Lewis shale shows significant change
in the behavior between 1.5 and 2.0 kilobars (Figure 25). At 1.5 kilobars
confining pressure of the Lewis shale still fails by brittle fracture; at
2 kilobars, the shale has become ductile and shows no drop in stress at
failure. This is typical of a shale unit. In contrast, the Picture Cliffs
sandstone (Figure 25), shows a continued brittle failure mode above 2 kilobars
confining pressure. Both the sandstone and shale tests were conducted at
in situ saturation levels; 2.5% and 1.7% water, respectively, for the
sandstone and shale. Failure envelopes for both intact and failed Lewis
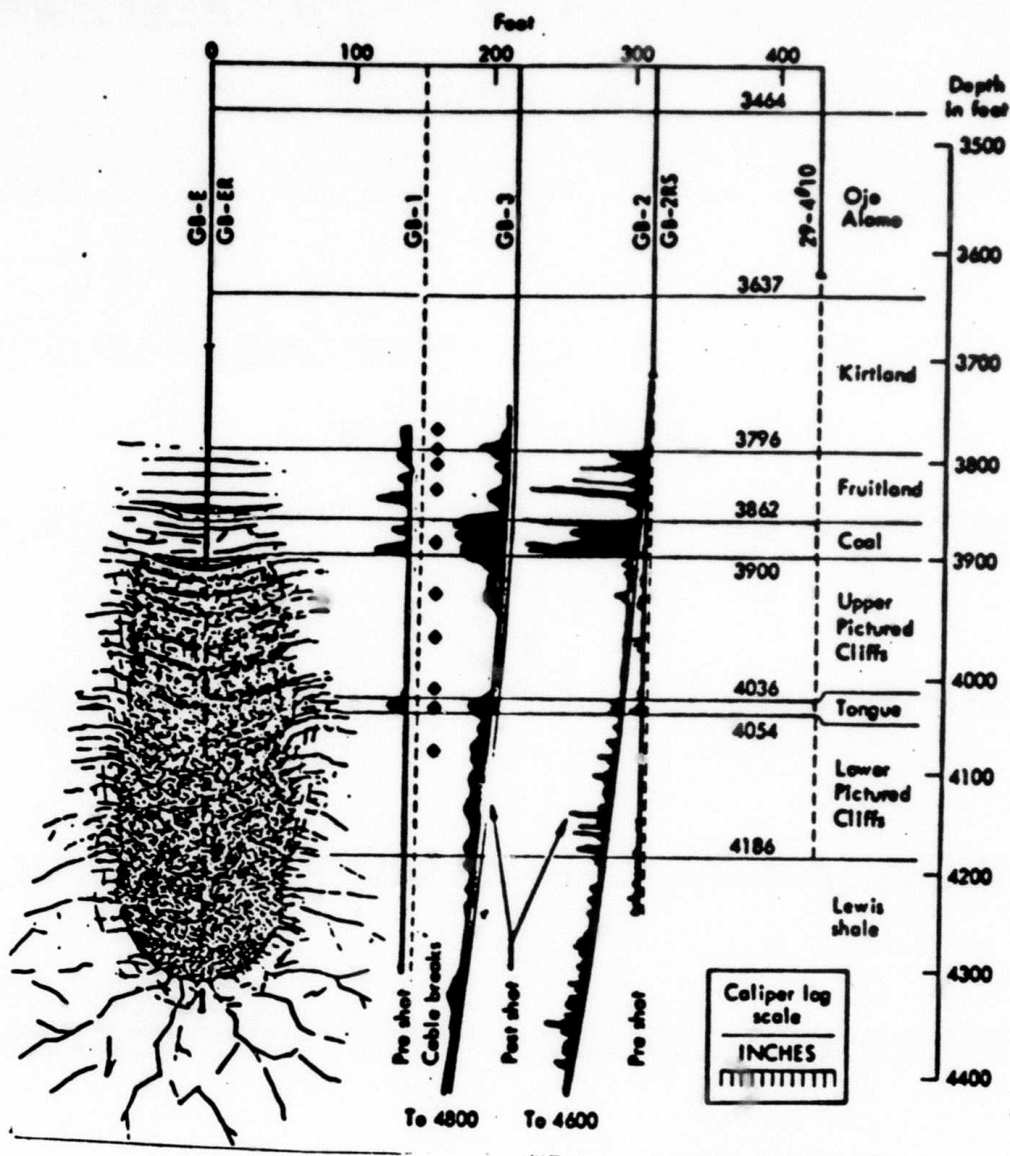
32

Figure 21. Schematic cross-section through GASBUGGY. The scale of this figure is approximate only. The results of pre-shot and post-shot caliper logs, giving an indication of the fractured nature of the formation are shown.

33

TABLE 6

PHYSICAL AND MECHANICAL PROPERTIES
OF GASSBUGGY MATERIAL

Property	Picture Cliffs Sandstone	Lewis Shale	
ρ bulk	2.443[1]	2.586[1]	gm/cc
ρ grain	2.52[2]	2.62[2]	gm/cc
% water	2.5[1]	1.7[1]	
V_p	11,200[2]	13,120[2]	km/s
V_s	8,100[2]	8,040[2]	km/s
ν	.16[1]	.16[1]	
k	.10-.16[2]		md

1. Holzer, F. [27]

2. Cherry, J. [28]

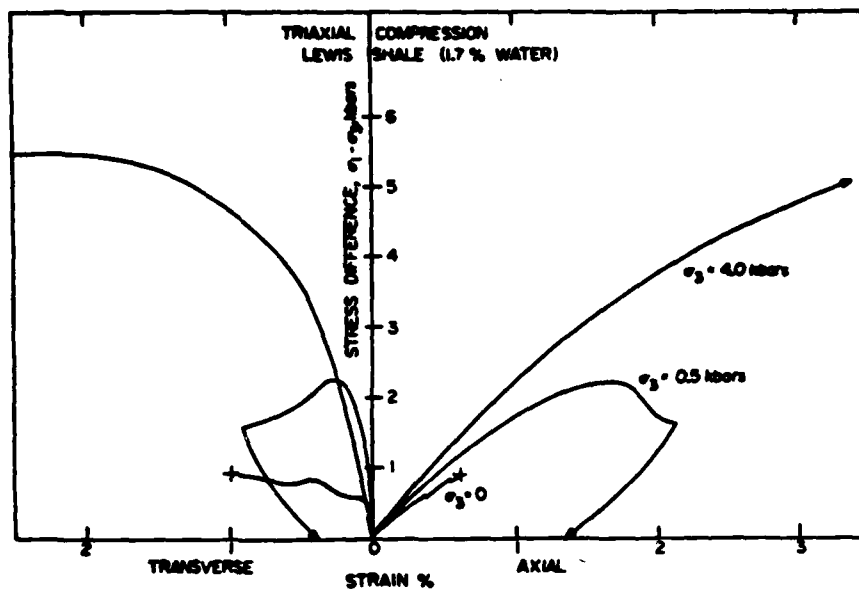34

Figure 22.   Stress difference vs. axial strain response of
             the Lewis shale.
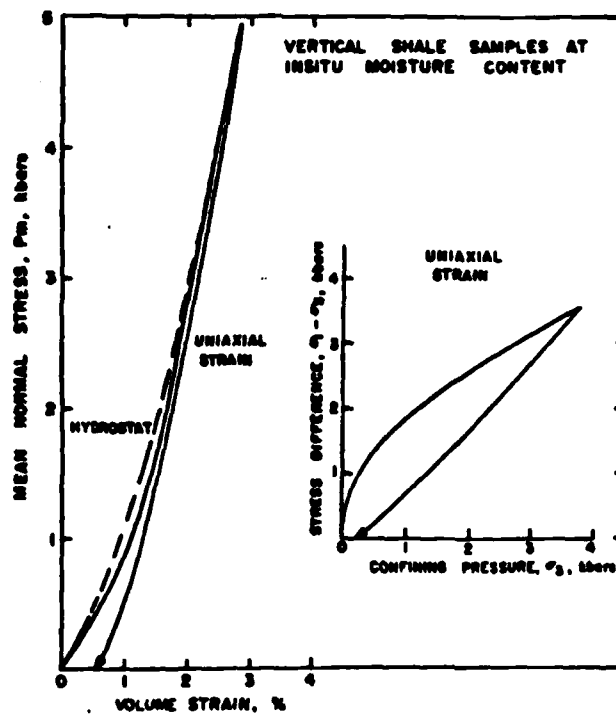

Figure 23.   The hydrostatic and uniaxial strain response
             of Lewis shale. Plots are of volume strain as a
             function of mean normal stress and stress difference
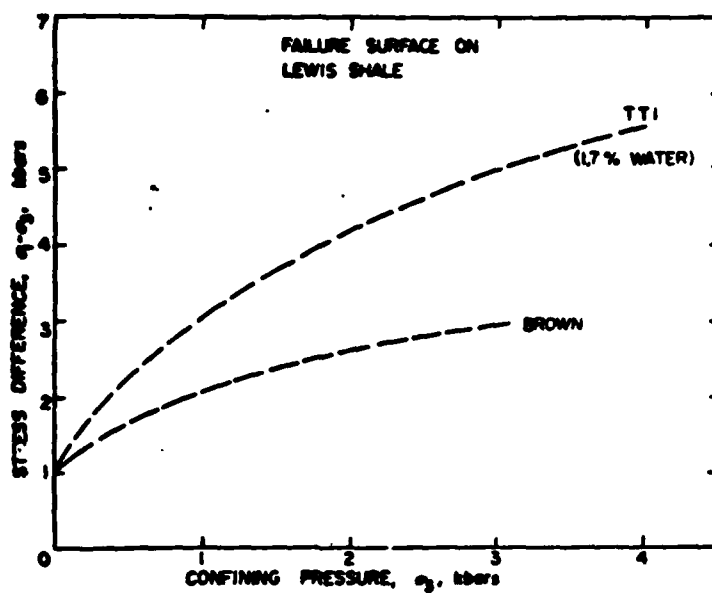   vs. confining pressure.

·35

Figure 24. Failure envelope of Lewis shale - Terra Tek (TTi),
failure envelope of 1.7% water. Failure envelope
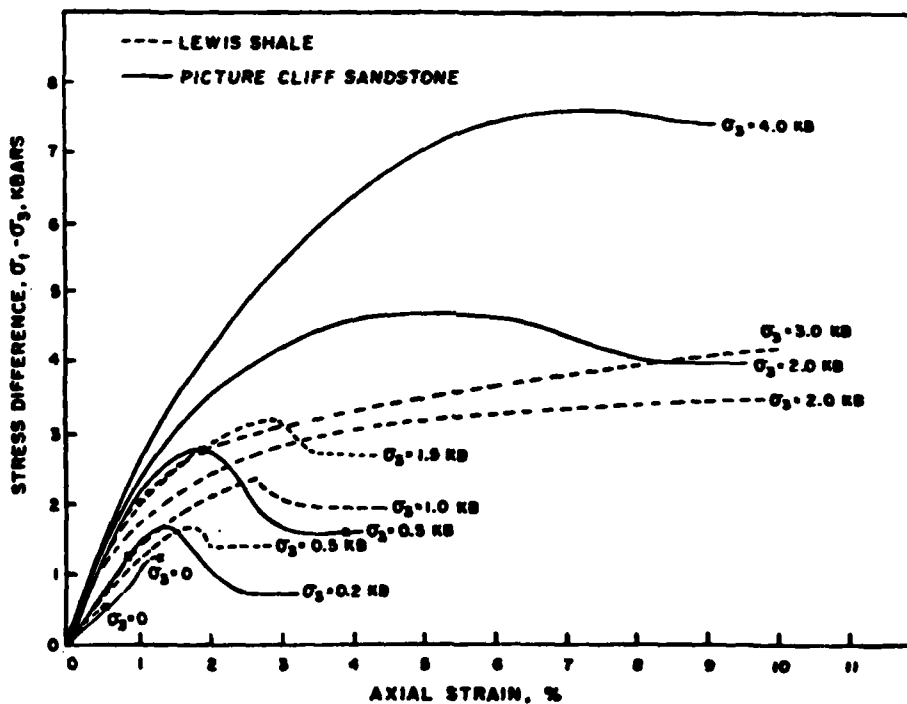from Brown with probably a higher water content.

Figure 25. The stress-strain response of Lewis shale and Picture
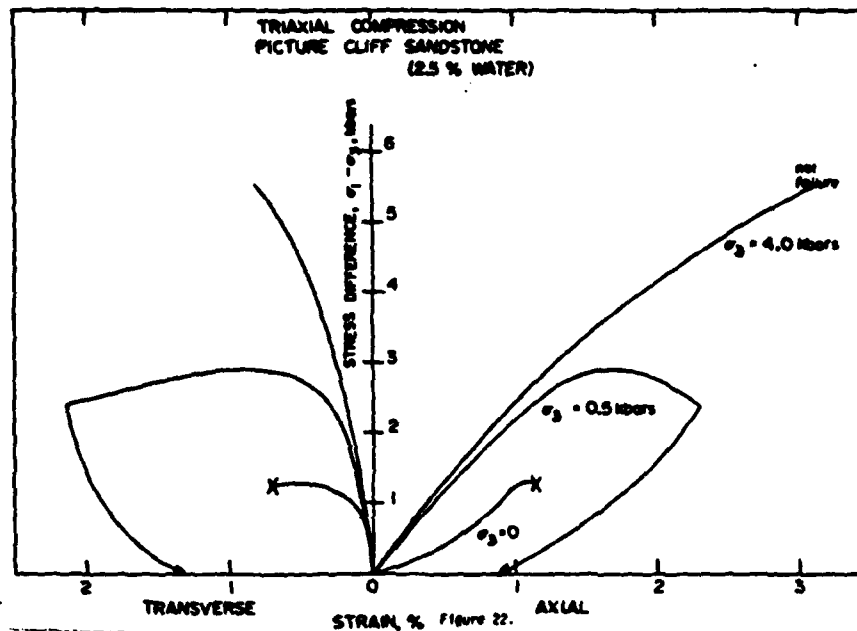Cliff sandstone up to 4 kilobars confining pressure.

36

Figure 26.   The stress-strain response of the Picture Cliff sandstone
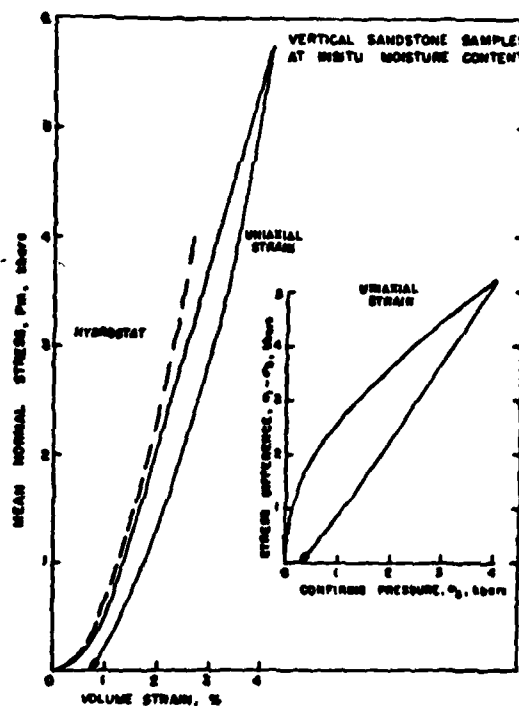up to 4 kilobars confining pressure.

Figure 27.   The hydrostatic and uniaxial strain response of Picture
Cliff sandstone.   The hydrostat and uniaxial strain response
plotted as a function of volume strain vs. mean normal stress
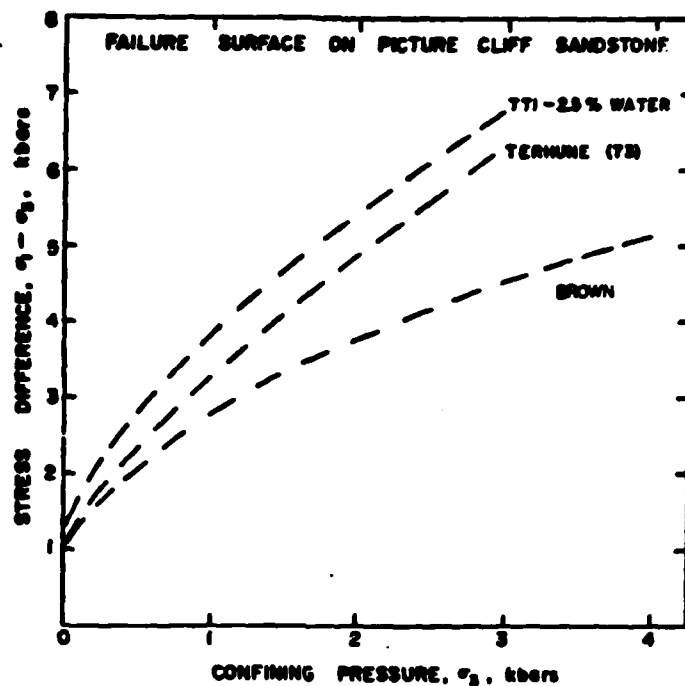and stress difference vs. confining pressure.

37

Figure 28. Failure envelope of Picture Cliffs sandstone
from three sources of data.

shale and the Picture Cliffs sandstone are shown in Figures 29 and 30.
For the Lewis shale and the residual failure envelope approaches that of
the intact failure envelope a little over 2 kilobars, but in the Picture
Cliffs sandstone difference between the initial and residual failure
envelopes remains appro mately constant and it would not be expected to
intersect until very high pressures where the two curves might merge as
shown that for brittle granites. For the Westerly granite, the two
failure envelopes do not merge until almost 17 kilobars confining pressure.[27]
A compilation of the failure envelopes for both the Lewis shale and the
Picture Cliffs sandstone indicated that the sandstone is stronger at
all confining pressures as would be expected (Figure 31). The shale
envelopes fall significantly below the sandstone envelopes especially at
confining pressures above 2 kilobars where the shale has become ductile.

Figure 30. Intact and residual failure envelopes for Picture Cliff sandstone. Note: the two curves are approximately parallel over the range of tests confining pressures studied.
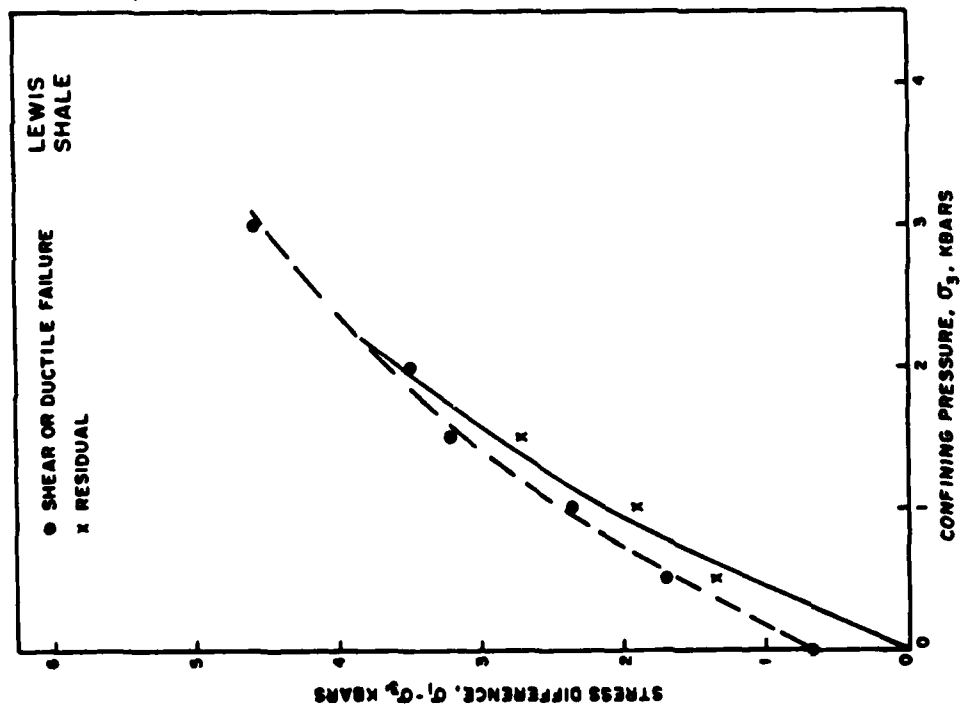

Figure 29. The intact and residual failure envelopes for Lewis shale. Note: the two curves come together at a little over 2 kilobars.

39

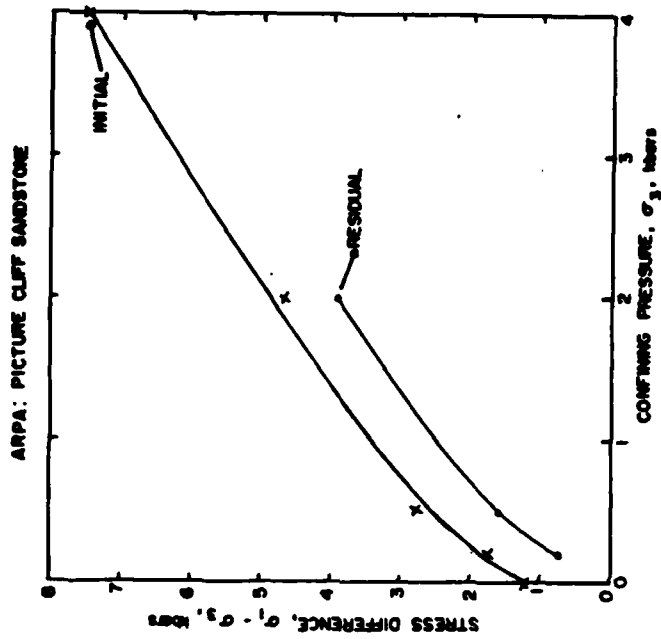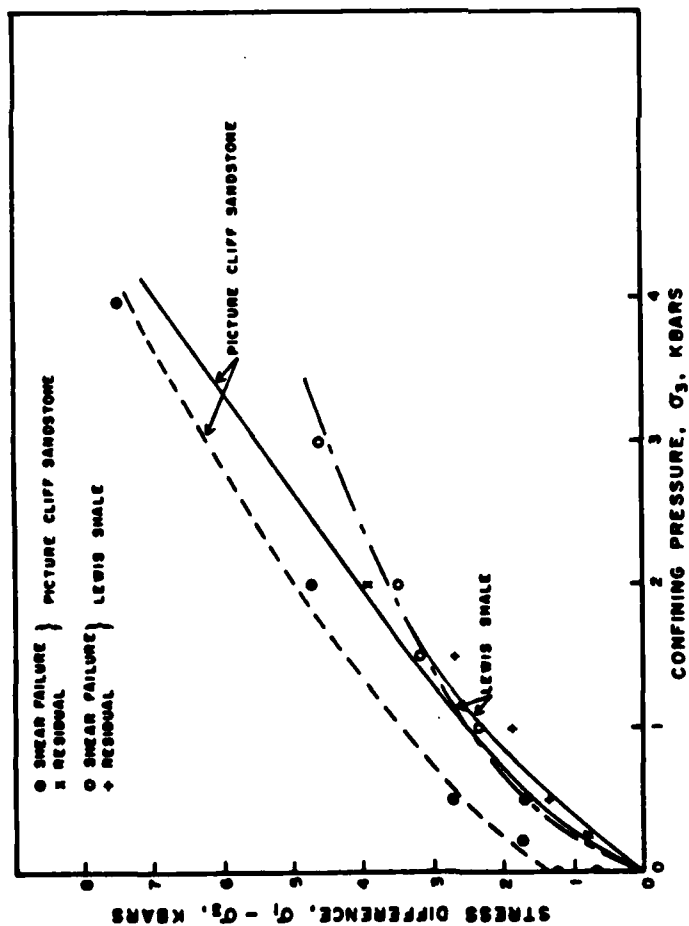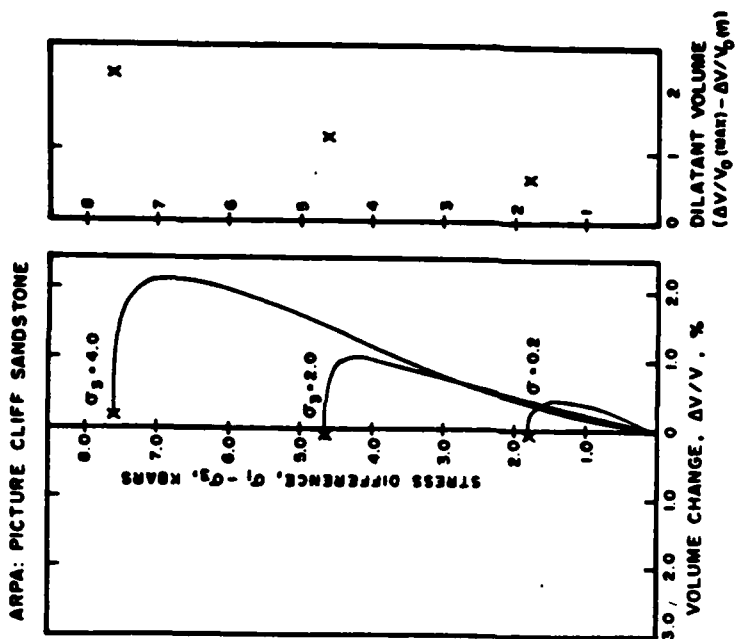Figure 32. The stress difference vs. volume strain plots illustrating the dilatant volume change occurring in the sandstone.

Figure 31. A summary plot of the intact and residual failure envelopes for Lewis shale and Picture Cliff sandstone.

Dilatancy: The role of dilatancy has important implications on the modeling
of material behavior. Dilatant volume represents an available void space
prior to failure. This effect coupled with the degree of saturation and
permeability will determine the role of pore pressure (effective stress)
and the ultimate strength of a material under *in situ* conditions. The plots
show the amount of dilatant volume for the sandstone and the shale as a
function of stress difference (Figures 32 and 33). As would be expected,
the sandstone undergoes an increased dilatancy with confining stress to a
maximum of 2.25% at a confining of 4.0 kilobars, a stress difference of 7.1
kilobars (Figure 32). This is significantly more than the dilatant volume
for the shale although it is very difficult to pick the failure point of
the shale because of its ductile nature beyond the 2 kilobars (Figure 33).
In fact, the meaning of dilatant volume for a ductile material such as
shale is open to questions since experimentally the failure is continuous
shearing without a large stress drop.

Strain Path Effects: A series of tests on both the Lewis shale and Picture
Cliff sandstone was conducted along special strain paths dictated by the
calculations of Pacifica Technology (PACTECH)[29]. The results of two sand-
stone tests are shown as plots of stress difference versus confining pressure
and confining pressure versus axial strain (Figures 34 and 35). These tests
were conducted following the test procedures outlined previously. The strain
paths are labeled in both of the diagrams so that a cross correlation can
be made between the two plots.

The sandstone sample was loaded hydrostatically to 0.2 kb and then
triaxially to 2.0 kb following prescribed strain paths. The maximum axial
strain was 2.75% which equated to a stress difference of 3.5 kilobars.

41

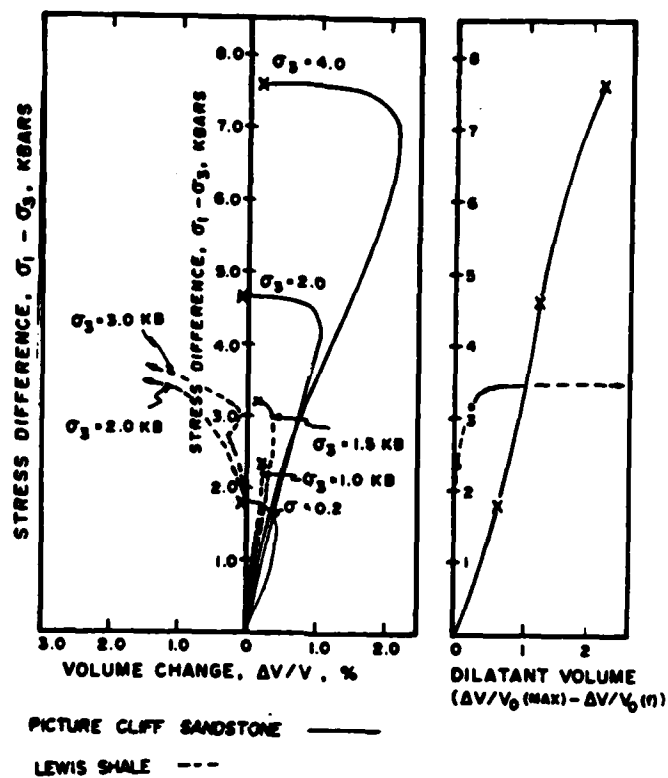Figure 33. Dilatant volume change as a function of stress difference for the Picture Cliff sandstone and Lewis shale. Note: the difference in the dilatant volume response of the two materials.
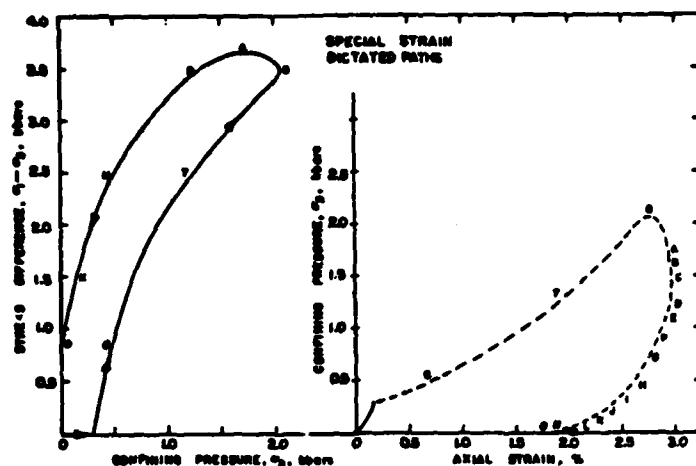
Figure 34. Strain paths loading of Picture Cliff sandstone
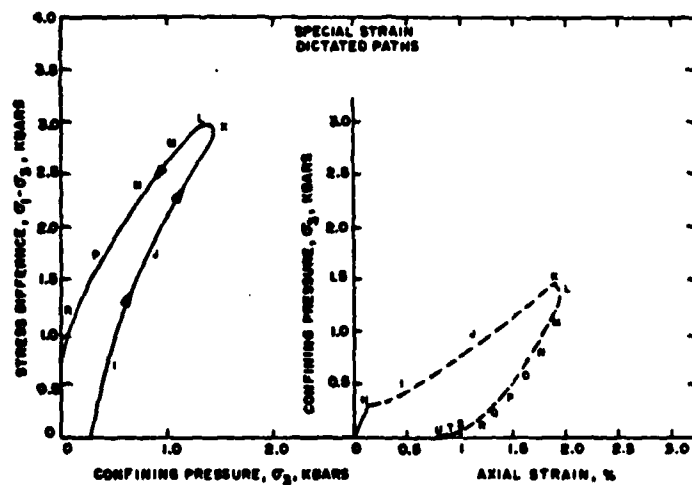simulating calculational load path responses
by PACTECH.

Figure 35. Strain path loading of Picture Cliff sandstone
simulating calculational load path responses
by PACTECH.

43

Upon unloading along strain path A-0, the resulting stresses increase to
3.7 kb at A and they decreased along the A-0 path in stress space. Note the
stress unloading path is to the left of the loading path indicating that
the rock can support a larger stress difference at a lower confining pres-
sure during the unloading cycle as indicated by the strain path. A
second set of dictated special strain paths for the Picture Cliffs sand-
stone conducted a lower confining pressure and resulted in stress
differences of only 3 kilobars and maximum axial strain of 2%. Again
this test was run by subjecting the sample to the hydrostatic confining
pressure to approximately 0.3 of a kilobar and then applying a triaxial
loading condition up to about 3 kilobars. The results of these tests
were then used to iterate back and forth between Terra Tek and the
calculational efforts of Pacifica Technology.

In summary, we looked at and compared several different types of
material property phenomena with respect to Lewis shale and the Picture
Cliffs sandstone. (1) The Lewis shale becomes ductile above 2 kilobars
while the Picture Cliffs sandstone still retains its brittle failure mechan-
ism up to at least 4 kilobars. (2) The residual failure for the shale
merges with the intact failure envelope at approximately 2 kilobars while
for the sandstone the residual and intact failure envelopes remain essen-
tially parallel up to the highest confining pressures tests (4.0 kilobars).
(3) The dilatant behavior of the sandstone is well defined and of course
increases with increasing confining pressure. It is more difficult to
ascertain the amount of dilatancy prior to failure of the Lewis shale because
of the ductile nature of the material above 2 kilobars. However, the shale

44

undergoes significantly less dilatancy than the sandstone at a given
confining pressure until the shale becomes ductile. (4) The compaction
under loading of both the sandstone and the shale is quite small due
to their low porosity, however under hydrostatic loading the shale is
stiffer than the sandstone although it is not able to support as high
a differential stress at a given confining pressure as the sandstone.

Strain Rate Effects on Modulus: The effect of strain rate on the dynamic
modulus of rock may be important to the development of a realistic
constitutive model for rock masses[30]. Strain rate effects may be seen
under conditions of stress relaxation under constant strain and creep
under constant. To analyze these effects we (1) developed an analytical
model of a viscoelastic standard solid (2) developed a test technique
and experimental apparatus to measure the relaxation modulus (E_t).
The model development is given in detail in Appendix A. An experimental
apparatus was developed to load a specimen in a 1.-10 millisecond rise
time to a few bars by dropping a suspended weight on to the specimen
and analyzing the stress relaxation with a laser interferometer. A
schematic of the experimental is given in Figure 36 and a photograph of
the apparatus in Figure 37.

Representative data from tests on Picture Cliffs sandstone are given
in Figures 38 and 39 respectively. The data for the sandstone shows a
rise time of 6 milliseconds to a stress level of 9.3 bars and for the
shale, a rise time of 2.3 milliseconds to $\sigma = 9.3$ bars. From the model
the relaxation modulus was calculated for the sandstone as follows:

Figure 37. Photograph of experimental apparatus with tests specimens.

OPTICAL DETECTOR

SCOPE

LENS

ADJUSTABLE MIRROR

~7.0"

FLAT ROCK

AIR SACKS

15.0"

2.0"

LENS

BEAM SPLITTER

SAMPLE

1.0"

6.0"

65 lb WEIGHT

STEEL CYLINDER

LASER

ADJUSTABLE PLATFORM

Figure 36. Schematic diagram of the experimental apparatus for the measurement of low stress level dynamic modulus.

46 />

46

ARPA INTERFEROMETER DATA
EL PASO SANDSTONE
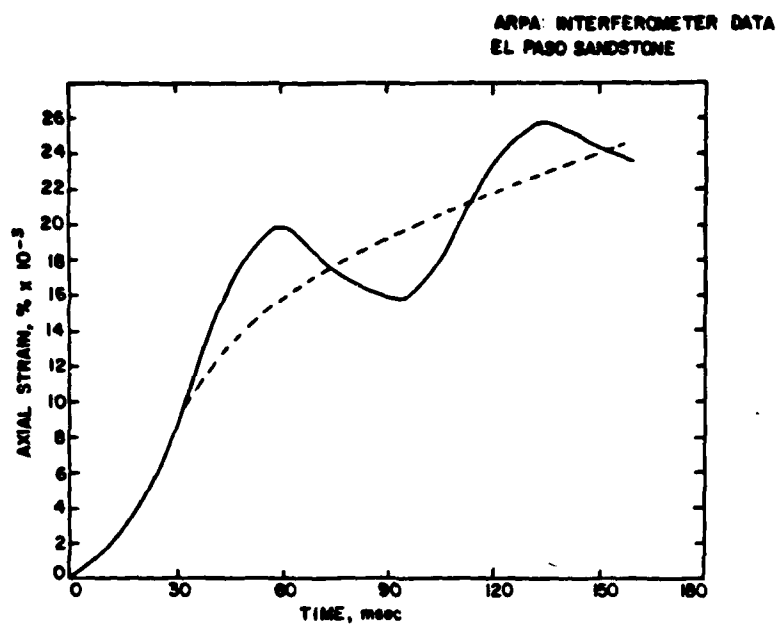
Figure 38. Axial strain vs. time for the low stress level dynamic tests on Picture Cliff sandstone.

ARPA INTERFEROMETER DATA
EL PASO SANDSTONE

Figure 39. Displacement vs. time for the low stress level dynamic tests conducted upon the Picture Cliff sandstone.

47

From the experiment:

$$t_0 = 6 \text{ msec}$$

$$\tan \alpha = 10 \text{ } \mu s/msec$$

$$\varepsilon(\infty) = 80 \text{ } \mu s$$

$$\varepsilon(t_0) = 63 \text{ } \mu s$$

$$\sigma_0 = 135 \text{ lb/}\dot{m}^2$$

Then:

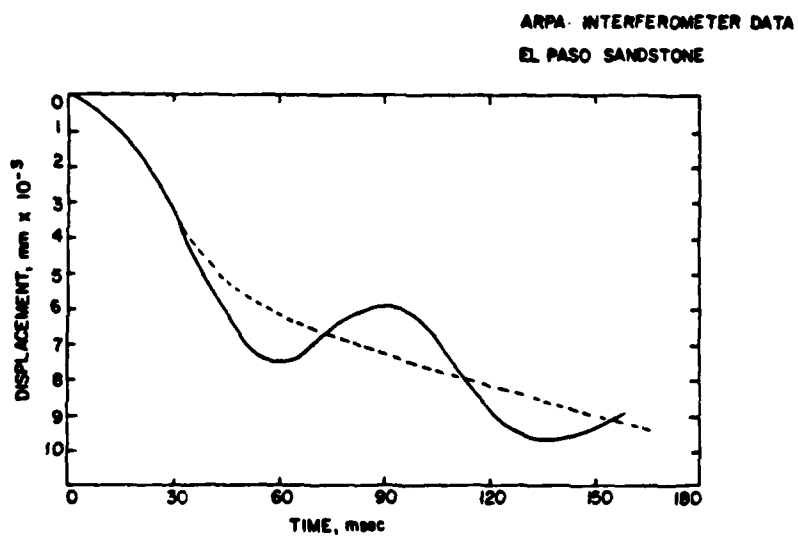$$\tan \alpha = \frac{\sigma_0}{t_0 R_1}$$

$$\varepsilon(\infty) = \sigma_0 \left[\frac{1}{R_1} + \frac{1}{R_2} \right]$$

$$\varepsilon(t_0) = \frac{\sigma_0}{t_0} \left[\frac{t_0}{R_1} + \frac{t_0}{R_2} - \frac{\eta}{R_2^2} + \frac{\eta}{R_2^2} e^{\frac{-R_2}{\eta} t_0} \right]$$

$$R_1 = \frac{\sigma_0}{t_0 \tan \alpha} = 2.25 \times 10^6 \text{ lbs/in}^2$$

$$R_2 = \frac{\sigma_0}{\varepsilon(\infty) - \frac{\sigma_0}{R_1}} = 6.75 \times 10^6 \text{ lb/in}^2$$

Solving (3) for η gives:

$$0 = 3.469 \times 10^7 - \eta + \eta e^{\frac{-40.5 \times 10^6}{\eta}}$$

$$\eta = 1.27 \times 10^8$$

Relaxation Modulus

$$E_{(t)} = 1.687 \times 10^6 (1-e^{-0.07t}) + 2.25 \times 10^6 e^{-0.07t}$$

$$E_{(t)} = 5.63 \times 10^5 e^{-0.07t} + 1.687 \times 10^6$$

Using the following values for the shale:

$$t_0 = 2.3 \text{ msec}$$

$$\tan \alpha = 8 \text{ } \mu s/msec$$

$$\varepsilon(t_0) = 18.5 \text{ } \mu s$$

$$\varepsilon(\infty) = 23 \text{ } \mu s$$

$$\sigma_0 = 135 \text{ lb/in}^2$$

$$E_{(t)} = 1.46 \times 10^6 e^{-0.02t} + 5.87 \times 10^6$$

A comparison of the moduli from static, impact and ultrasonic (dynamic) tests are summarized in Table 7. For both the Lewis shale and Picture Cliff sandstone the static moduli was considerably less than the dynamic moduli. In the case of the Picture Cliff sandstone it was a factor of 2 less (76 vs. 152 kb) than impact test results and almost a factor of three less than moduli calculated from ultrasonic tests. The data from the Lewis shale also indicates a significant difference between static and dynamic moduli. However, the impact tests gave a higher value than the ultrasonic data for the Lewis shale. Aluminum was used as a calibration sample for comparison with published data.

TABLE 7

Modulus Comparisons

Material	Test Type	Young's Mod (kbars)
Picture Cliff Sandstone (dry)	Static	76
	Impact	152
	Ultrasonic	221
Lewis Shale (dry)	Static	159 for stress < 500 psi
		338 for stress > 500 psi
	Impact	503
	Ultrasonic	400
Aluminum	Impact	690

In summary, the experimental technique proved moderately successful and values of relaxation modulus were obtained in the loading range 2-6 msec. Improvement in the loading mechanism is required so that ringing does not occur. In addition more rapid loading in a 1.0 msec. risetime would be beneficial as would a method to vary the loading rate equivalent to a frequency range of 5-100 Hz. in order to better evaluate rate effects.

3.4 Salt

The physical and mechanical properties of bedded salt from the GNOME event and dome salt from the SALMON event were obtained. The physical properties are listed in Table 8. These properties can be compared to data on a variety of salt types (bedded, domal, polycrystalline, single crystal) obtained from the literature (Table 9).

The mechanical properties were obtained under both triaxial compression and extension. Plots of axial stress at various confining pressures indicates that salt becomes ductile at approximately 1.5% strain even at very low confining pressures (250 psi) (Figure 40). Triaxial tests up to a confining pressure of 4 kilobars indicates that both bedded and dome salt are "ductile" at a confining pressure of 0.75 kb and reached maximum stress difference of 0.68 kb (Figure 41). This is slightly less strength (12%) than the 0.8 kb measured for the ultimate strength of polycrystalline salt measured previously. Heard's data also indicated that ultimate strength was independent of strain above 2% strain (Figure 42) for polycrystalline salt[36].

TABLE 8

PROPERTIES OF GNOME AND SALMON SALTS

	GNOME[1]	GNOME[2]	SALMON[3]	SALMON[4]
ρ_o (gm/c)	2.13-2.46	2.136	1.89	2.214
ρ_{grain} (gm/cc)	---	2.173	----	2.236
Porosity	.76-5.1	1.730	----	1.000
% water	1.00	.026	----	.019
V_p (km/sec)	4.08		4.30	
V_s (km/sec)	2.88		2.35	
K (kbar)			2.31	
G (kbar)			1.20	
ν	0.28-0.32		0.26	
Depth (m)		309.45		790.55

[1]Weart (1963)[31], [2]Pratt, et al. (1978), [3]Christensen (1964)[32]

[4]Pratt, et.al. (1978)

51

TABLE 9

REPRESENTATIVE SALT PROPERTIES

PROPERTY	UNITS	DOME	BEDDED	POLY XTAL.	SINGLE XTAL.
ρ bulk	gm/cm³	2.16[3] 2.17[6]	2.17(w/clay)[7] 2.17(w/anhy)	2.14[4]	
porosity	%		0.5[7]	1.11[4] 4.16[8]	
σ_{ult}	kbars	0.38[1] 0.14[2] 0.20[2] 0.21[3] 0.27	0.27±.03(⊥)[1] 0.29±.03(‖)[1] 0.16±.03(w/clay)[7] 0.25±.04(w/anhy)[7] 0.44(3=0.03)[6]	0.56[4]	0.26(1 samp)[5]
T_o	kbars	0.008[3]	0.014±.003(w/clay)[7] 0.016±.001(w/anhy)[7]	0.038[4]	0.42(2 samp)[5]
V_p	km/s	4.1[3] 4.2(.051kb)[3]		4.1[4] 4.4(0.48kb)[4]	
V_s	km/s			2.4[4] 2.7(0.48kb)[4]	
E_t	kbars	39±3' 54 to 120[2] 95 to 160[2] 110(10% ult)[3]	24±12 (⊥)[1] 2±4 (‖)[1] 140±40(w/clay)[7]	120(initial)[8]	
μ (shear)	kbars			136(initial)[4] 122(dynamic)[4] initial	
ν	-	0.19(initial)[3] 0.35(10% ult)[3]	0.18-0.27[7] 0.22	0.28(static)[4] initial 0.23(dynamic)[4] initial	
σ yield pt.	kbars	0.20[1] 0.082[2] 0.12[2] 0.10[3]	0.16±.02 (⊥)[1] 0.17±.03 (‖)[1]	0.14[8] initial	0.075[5]
k(bulk)	kbars	37-56(init)[2] 58(initial)[2]		211(triaxial)[4] initial 109(hydrostatic) initial 184(dynamic)[4] initial	238(hyd.init)[4]

[1] Pariseau, W.[33]

[2] Serrata, S.[34]

[3] Deere, D.[35]

[4] Heard, H.[36]

[5] Handin, J.[37]

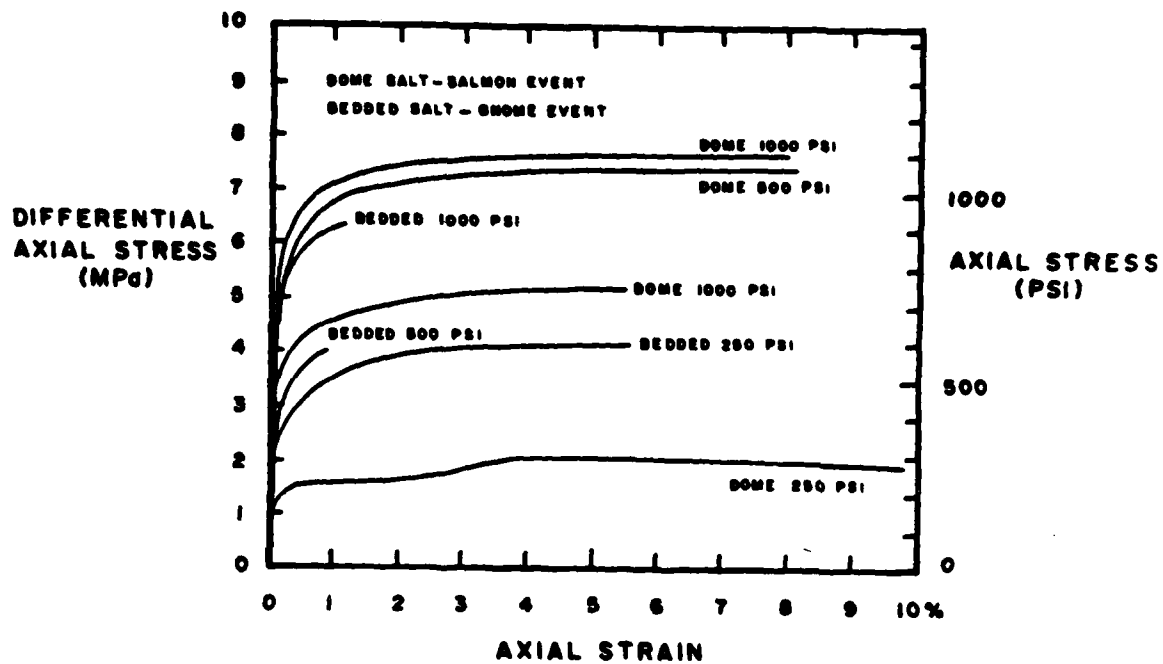[6] Hansen, R.[38]

[7] Wawersik[39]

[8] Dropek, R.[40]

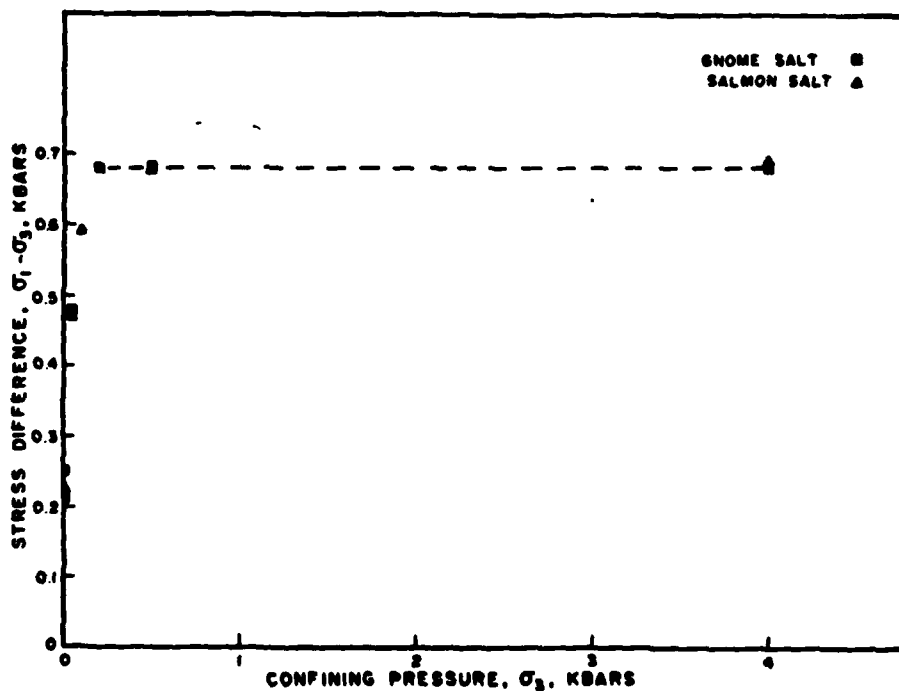Figure 40. Stress-strain response of bedded and dome salt at various confining pressures.

Figure 41. Failure envelopes for GNOME (bedded salt) and SALMON (domal salt) as a function of confining pressure up to 4 kilobars.
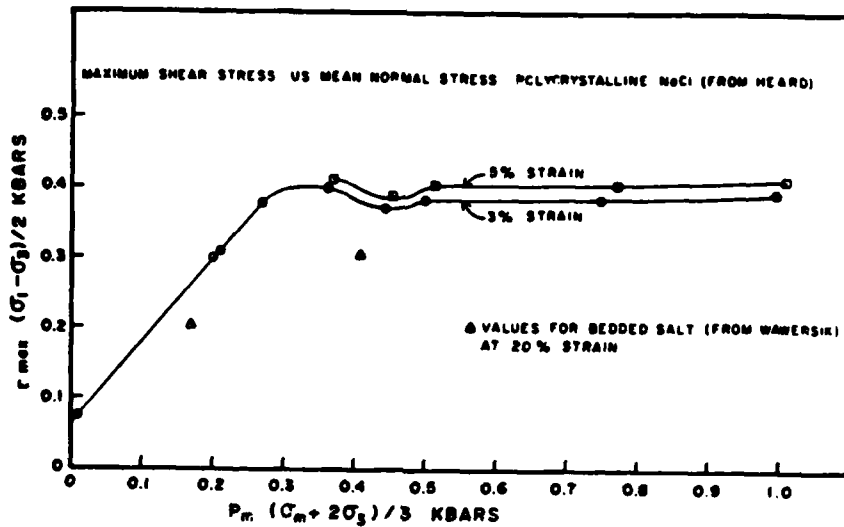
Figure 42. Failure envelope of polycrystalline salt plotted as maximum shear stress vs. mean normal stress at constant strain values[36].

Cylindrical samples nominally 1 inch (25 mm) in diameter by 1.5 inch (37 mm) in length were tested in extension with confining pressure of 250, 500 and 1,000 psi (1.72, 3.45 and 6.89 MPa respectively). The specimen ends were surface ground flat and parallel to within ±.01 mm and the specimens were jacketed with a double layer of polyurethane, .01 inch (.25 mm) thick. Steel end caps were attached to the specimens with 5 minute epoxy and axial strain cantilevers were attached to the end caps with set screws. A hook was attached to the bottom end cap and a universal joint and loading piston were attached to the top.

The specimen assembly was then lowered into a small pressure vessel and rotated 90° to engage the hook into its seat in the bottom of the vessel. The upper loading piston provided the seal at the top of the vessel by engaging 2 O-rings.

The pressure required to overcome the seal friction was measured to be about 200-250 psi (1.4-1.7 MPa) over the range of confining pressure used. The hydraulic ram from the testing machine frame was then lowered to touch the top of the loading piston and the confining pressure raised to the desired value. Then the ram was raised at 1.5×10^{-3} in/sec, allowing extension of the specimen at the nominal strain rate of 10^{-3} sec^{-1} until failure.

The combinations of the seal friction and electronic noise resulting from the extremely low differential axial load required for extension of such a small specimen résulted in an overall uncertainty in the differential axial stress measurement of about 250 psi (1.72 MPa).
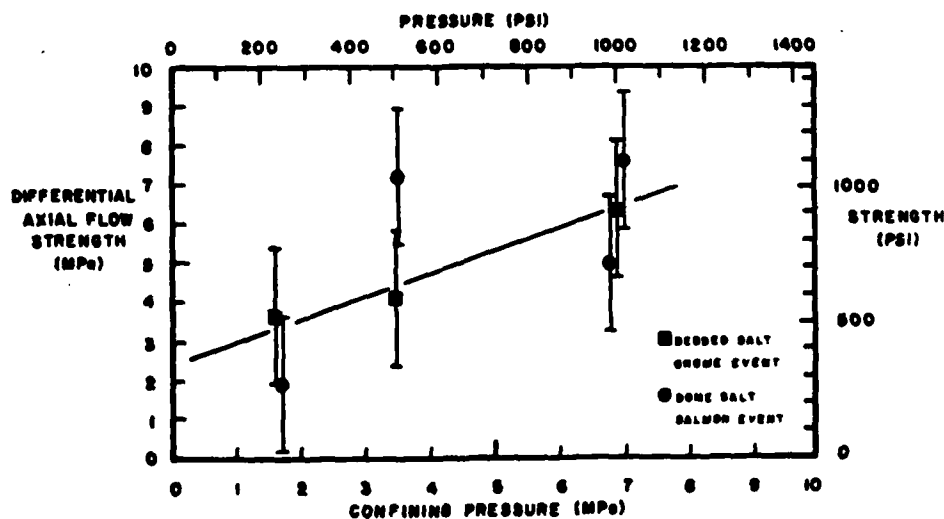
Figure 43. Extension failure envelopes. Differential axial strength as a function of confining pressure for both bedded and domal salt.

The extension failure envelopes (Figures 43) shows an increase in strength with confining pressure up to 7 MPa (70 bars). The average strength is approximately 6.2 MPa (62 bars) at 7.0 MPa confining stress. The data scatter is significant due to the nature of salt. With the wide scatter in the data as indicated by the bars, there is no indication that one kind of salt (bedded vs. dome) is stronger in extension than the other.

APPENDIX A

STRESS-STRAIN RESPONSE OF VISCOELASTIC STANDARD SOLID MODEL

Standard Solid Viscoelastic Model

Strain rate effects seen in rocks when stresses are applied are manifested by stress relaxation under constant strain and creep under constant stress. Mathematically, this response can be modeled by combining various systems of linear springs and viscous dash pots. One such model is the standard solid model as shown below in Figure A.
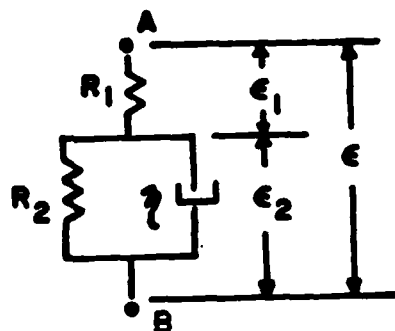
R - Elastic spring constant

η - Co-efficient of viscosity

ϵ - Strain

The standard solid model is simply a linear spring in series with a Kelvin model (spring and dash plot in parallel). Constitutive equations for this viscoelastic model are developed as follows:

When a stress is applied across the sample at points A and B, time dependent strain results. Total strain at any time (t) is the sum of the individual element strains.

$$\epsilon = \epsilon_1 + \epsilon_2 \tag{1}$$

where

For the spring
$$\epsilon_1 = \frac{\sigma}{R_1} \tag{2}$$

And for the Kelvin element

$$\dot{\varepsilon}_2 + (R_2/\eta)\,\varepsilon_2 = \frac{\sigma}{\eta} \qquad (3)$$

In the LaPlace space

$$\hat{\varepsilon}_1 = \frac{\hat{\sigma}}{R_1} \qquad (4)$$

$$\hat{\varepsilon}_2 = \frac{\hat{\sigma}}{\eta(S + \frac{R_2}{\eta})} \qquad (5)$$

so

$$\hat{\varepsilon} = \frac{\hat{\sigma}}{R_1} + \frac{\hat{\sigma}}{\eta(S + \frac{R_2}{\eta})} \qquad (6)$$

Rearranging

$$\frac{\eta}{R_2}\,S\hat{\varepsilon} + \hat{\varepsilon} = \frac{\hat{\sigma}}{R_1} + \frac{\eta}{R_1 R_2}\,S\hat{\sigma} + \frac{\hat{\sigma}}{R_2} \qquad (7)$$

Taking the inverse LaPlace

$$\frac{\eta}{R_2}\,\dot{\varepsilon} + \varepsilon = \frac{R_1 R_2}{R_1 R_2}\,\sigma + \frac{\eta}{R_1 R_2}\,\dot{\sigma} \qquad (8)$$

Rearranging to general differential equation form

$$\sigma + \frac{\eta}{R_1 + R_2}\,\dot{\sigma} = \frac{R_1 R_2}{R_1 + R_2}\,\varepsilon + \frac{R_1 \eta}{R_1 + R_2}\,\dot{\varepsilon} \qquad (9)$$

Relaxation Modulus

In a relaxation test a step of constant strain $\varepsilon = \varepsilon_0 H(t)$ is applied and the stress $\sigma(t)$ is measured as shown in Figures B and C. If the material behavior is linear, the stress can be represented by:

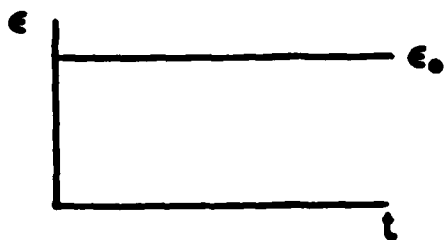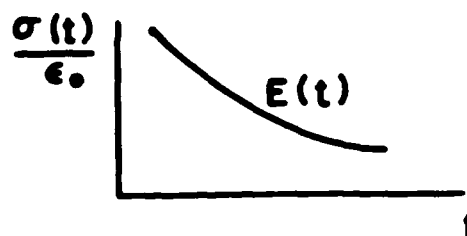$$\sigma(t) = \varepsilon_0 E(t) \qquad (10)$$

58

Figure B

Figure C

The function $E(t)$ thus obtained is called the relaxation modulus. It is the stress per unit of applied strain and is different for each material.

Inserting a unit step of strain into the standard solid differential equation (9) yields

$$\sigma + \frac{\eta}{R_1 + R_2} \dot{\sigma} = \frac{R_1 R_2}{R_1 + R_2} \epsilon_0 H(t) + \frac{R_1 \eta}{R_1 + R_2} \epsilon_0 \delta(t) \tag{11}$$

In the LaPlace space

$$\sigma + \frac{\eta}{R_1 + R_2} (S) \hat{\sigma} = \frac{R R}{R + R} \left(\frac{1}{S}\right) \epsilon_0 + \frac{R_1 \eta}{R_1 + R_2} \epsilon_0 \tag{12}$$

or

$$\hat{\sigma} = \left[\frac{\frac{R_1 R_2}{R_1 + R_2} \left(\frac{1}{S}\right) + \frac{R_1 \eta}{R_1 + R_2}}{1 + \frac{\eta}{R_1 + R_2} S} \right] \epsilon_0 \tag{13}$$

Taking the inverse LaPlace and arranging terms

$$\sigma(t) = \left[\frac{R_1 R_2}{R_1 + R_2} + \left(R_1 - \frac{R_1 R_2}{R_1 + R_2}\right) e - \left(\frac{R_1 + R_2}{\eta}\right) t \right] \epsilon_0 \tag{14}$$

The relaxation modulus is therefore

$$E(t) = \left[\frac{R_1 R_2}{R_1 + R_2} + \left(R_1 - \frac{R_1 R_2}{R_1 + R_2}\right) e - \left(\frac{R_1 + R_2}{\eta}\right) t \right] \tag{15}$$

59

Experimental Determination of R_1, R_2 and η

To determine a numerical value for the relaxation modulus, the spring constants and coefficient of viscosity must be known. These values can be obtained from a creep or relaxation test. The test chosen was an impact test where a ramp stress followed by constant stress was applied and the resulting strain was measured. The test is represented in Figures D and E.
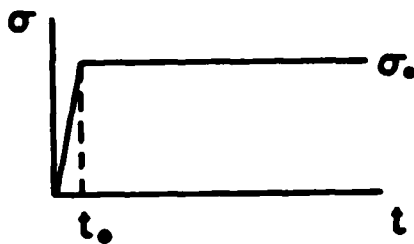
Figure D
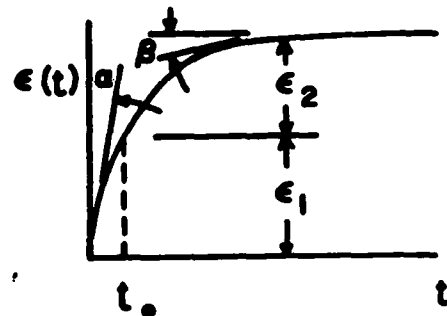
Figure E

From this test, one can measure α, β, $\epsilon(t)$ and $\dot{\epsilon}(t)$. Measurement of these quantities allows determination of R_1, R_2 and η as shown by the exact differential equations for this type loading.

For $t < t_0$

$$\sigma = \frac{\sigma_0}{t_0}\, t \tag{16}$$

$$\hat{\sigma} = \frac{\sigma_0}{t_0}\left(\frac{1}{s^2}\right) \tag{17}$$

Inserting into equation (6)

$$\hat{\epsilon} = \left[\frac{1}{R_1} + \frac{1}{\eta\,\frac{R_2}{\eta} + s}\right]\frac{\sigma_0}{t_0}\left(\frac{1}{s^2}\right) \tag{18}$$

60

Inverting from the LaPlace

$$\epsilon(t) = \frac{\sigma_0}{t_0} \left[\frac{t}{R_1} + \frac{t}{R_2} - \frac{\eta}{R_2^2} + \frac{\eta}{R_2^2} \, e - \frac{R_2 t}{\eta} \right] \qquad (19)$$

Differentiating

$$\dot{\epsilon}(t) = \left[\frac{\sigma_0}{t_0} \, \frac{1}{R_1} + \frac{1}{R_2} - \frac{1}{R_2} \, e - R_2/\eta^t \right] \qquad (20)$$

at $t = 0+$

$$\dot{\epsilon}(0+) = \frac{\sigma_0}{t_0 R_1} = \tan \alpha \qquad (21)$$

For $t > t_0$

$$\sigma = \frac{\sigma_0}{t_0} t - \frac{\sigma_0}{t_0} (t - t_0) \qquad (22)$$

$$\hat{\sigma} = \frac{\sigma_0}{t_0} \left(\frac{1}{S^2}\right) - \frac{\sigma_0}{t_0} \left(\frac{1}{S^2}\right) e^{-S t_0} \qquad (23)$$

Inserting into equation (6)

$$\hat{\epsilon} = \left[\frac{1}{R_1} + \frac{1}{\frac{\eta(R_2 + S)}{\eta}} \right] \left[\frac{\sigma_0}{t_0} \left(\frac{1}{S^2}\right) - \frac{\sigma_0}{t_0} \left(\frac{1}{S^2}\right) e^{-S t_0} \right] \qquad (24)$$

Inverting from the LaPlace

$$\epsilon(t) = \frac{\sigma_0}{t_0} \left[\frac{t_0}{R_1} + \frac{t_0}{R_2} + \frac{\eta}{R_2^2} \, e^{-R_2/\eta^t} (1 - e^{R_2/\eta^t}) \right] \qquad (25)$$

At $t = \infty$

$$\epsilon(\infty) = \sigma_0 \left[\frac{1}{R_1} + \frac{1}{R_2} \right] \qquad (26)$$

Differentiating

$$\dot{\epsilon}(t) = \frac{1}{R_2} \, e^{-R_2/\eta^t} (1 - e^{R_2/\eta^t}) \qquad (27)$$

61

At t = ∞

$$\dot{\epsilon}\,(\infty) = 0 = \tan\beta \qquad (28)$$

Thus, by substituting measured values of α, $\epsilon(t_0)$ and $\epsilon(\infty)$ into equations 19, 21 and 26, one can calculate numerical values for R_1, R_2 and η. These values can then be inserted into the relaxation modulus.

REFERENCES

1. Dropek, R. K., Butters, S. W. and Jones, A. H., "Methods for Determination of Physical Properties of Rock Materials," Terra Tek, Inc., TR 75-13, 1975.

2. Green, S. J., Griffin, R. M. and Pratt, H. R., "Stress-Strain and Failure Properties of a Porous Shale" (preprint SPE 4242), Soc. of Pet. Eng. of AIME, Dallas, Texas, pp. 117-128, 1973.

3. Schock, R. N., Abey, A. E., Bonner, B. P., Duba, A. and Heard, H. C., "Mechanical Properties of Nugget Sandstone," Lawrence Livermore Laboratory, UCRL - 51447, 19 p., 1973.

4. Isenberg, Jeremy, "A Sourcebook of Underground Phenomena and Effects of Nuclear Explosions," Part Two: "Mechanical Properties of Earth Materials," Nuclear Geophysics, Agbabian Associates, El Segundo, California, 150 p. 1972.

5. Brown, W. S. and Swanson, S. R., "Constitutive Equations for Westerly Granite and Cedar City Tonalite for a Variety of Loading Conditions," Final Report, University of Utah Mechanical Engineering Dept., DASA 2473, 118 p., 1970.

6. Stephens, D. R. and Lilley, E. M., "Loading-Unloading Pressure-Volume Curves for Rock," Proc. Symp. Engineering with Nuclear Explosives, U. S. Depart. of Commerce, Springfield, Virginia, 22151, Vol. 1, pp. 89-109, 1970.

7. Green, S. J., Butters, S. and Griffin, R., "High Pressure Mechanical Properties of the U12n.05 and U12t.02 Test Sites," Nevada Test Site, Terra Tek, Inc., TR 72-19, 1972.

8. Butters, S. W., Nielsen, R. R., Jones, A. H. and Green, S. J., "Material Properties of Grouts and of Tuffs from Selected Drill Holes," Terra Tek, Inc., TR 73-69, 1973.

9. Green, S. J. and Perkins, R. D., "Uniaxial Compression Tests at Varying Strain Rates on Three Geologic Materials," in Basic and Applied Rock Mechanics, AIMMPE, New York, pp. 35-54, 1972.

10. Cristman, D. R., et. al., "Measurements of Dynamic Properties of Materials," Experimental Methods and Techniques, DASA 2501-2, MSL-70-23, August 1971.

11. McQueen, R. G., Marsh, S. P. and Fritz, J. N., "Hugoniot Equation of State of Twelve Rocks," Jour. Geophys. Res., Vol. 72, No.20, pp. 4999-5036, 1967.

12. Brace, W. F. and Jones, A. H., "Comparison of Uniaxial Deformation in Shock and Static Loading of Three Rocks," Jour. Geophys. Res.,

13. Pratt, H. R., Black, A. D. and Brace, W. R., "Friction and Deformation of Jointed Quartz Diorite," Third Cong. Int. Soc. Rock Mech., Part A, pp. 306-310, 1974.

14. Goodman, R. E., "The Deformability of Joints in Determination of the In Situ Modulus of Deformation of Rock," ASTM STP 477, pp. 535-546, 1970.

15. Rosso, S., Simonson, E. R., Wawersik, W. and Jones, A. H., "Determination of the Properties of Jointed Oil Shale," Terra Tek, Inc., Report TR 74-60, Rec. 1974.

16. Goodman, R. E. and Ohnishi, Y., "Undrained Shear Tests on Jointed Rock," Rock Mechanics, in press, 1973.

17. Barton, N. R., "A Relationship Between Joint Roughness and Joint Shear Strength," Proc. Symp. on Rock Fracture, ISPM, Paper 1-8, 1971.

18. Pratt, H. R., Black, A. D. and Bonney, F. J., "Frictional Properties of Cedar City Quartz Diorite, Air Force Weapons Laboratory, AFWL TR-72-122, 1972.

19. Logan, J. M., Iwasaki, T., Friedman, M. and Ling, S. K., "Experimental Investigation of Sliding Friction in Multilithologic Specimens," in Geol. Factors in Rapid Excavation, Geol. Soc. Am. Eng. Geol. Case Hist. No. 9, p. 55-67, 1973.

20. Butters, S., et al., Field, Laboratory and Modeling Studies on Mount Helen Welded Tuff for Earth-penetrator Test Evaluation, Defense Nuclear Agency, DNA 4085 F, 1975.

21. Heard, H. C., "The Influence of Environment on the Inelastic Behavior of Rock," Proc. Symp. Engineering with Nuclear Explosives, U. S. Dept. of Commerce, Springfield, Virginia, Vol. 1, pp. 127-141, 1970.

22. Duba, A. H., Heard, H. C. and Santor, M. L., "Effect of Fluid Content on Mechanical Properties of Westerly Granite," Lawrence Livermore Laboratory, U. C. Livermore, UCRL - 51626, 1974.

23. Nordyke, M. D., "A Review of Soviet Data on the Peaceful Uses of Nuclear Explosives," Ann. Nuclear Energy, Vol. 2, p. 657-673, 1975.

24. Archambeau, C. and Sammis, C., "Seismic Radiation from Explosives in Prestressed media and the measurement of Tectonic Stress in the Earth," Reviews of Geophysics and Space Physics 8, p. 473, 1970.

25. Pratt, H. and Rawson, D., "Summary of the Geotechnical Workshop on Block Motion," DNA sponsored, March 14 and 15, 1977.

26. Pratt, H. R., Hustrulid, W. A. and Stephenson, D. E., "Earthquake
    Damage to Underground Facilities, Savannah River Laboratory
    DP-1513.

27. Horzer, F., GASSBUGGY preshot summary report, Lawrence Radiation Lab.,
    TID-4500, UC-35, Nov. 1967.

28. Cherry, J. T., Larson, D. B. and Rapp, E. G., "Computer Calculations
    of the GASSBUGGY event," Lawrence Radiation Laboatory, UCRL-50419,
    May, 1968.

29. Allen, R., "Briefing on RDP Material Property Dependence," DARPA
    Program Review Meeting, PT-U76-0053, April, 1976.

30. Bjork, R., personal communication, 1976.

31. Weart, W. D., "Particle motion near a Nuclear Detonation in Halite
    (Project GNOME Final Report), Sandia Rept. PNE-108F, 1963.

32. Christensen, D. M., "Quantitative Interpretation of 3-Dimensional
    Velocity Logs, Ann. Progress Report, March 1963-March 1964,
    Lawrence Radiation Laboratory, Birdwell D. J., Seis. Ser. Corp.,
    1964.

33. Pariseau, W., Thermo-elastic-Plastic finite Element Analysis of Under-
    ground Radioactive Waste Isolation Rooms. OakRidge Nat. Lab.
    Report., ORNL-LR-1650, Table 1, p. 64, 1975.

34. Serata, S., et al., "Theory of Aggregate Rock Behavior Based on Absolute
    Three-Dimensional Testing (ATT) of Rock Salt, PRoc. 10 Symp.
    Rock Mechanics, AIME, 431-473, 1972.

35. Deere, D. U. and Miller R. P., "Engineering Classification of Intact
    Rock", Air Force Weapons Laboratory, AFWL TR 65-116. 1966.

36. Heard, H. C., "Steady State Flow in Polycrystalline Halite at Pressures
    of 2 kilobars,", Geophysics Monograph Series V-16, 191-209, 1972.

37. Handin, J. and Hager Jr., R. V., Experimental Deformation of Sedimentary
    Rocks, Dec. 1958.

38. Hansen, F., and Gnirk, P. F., "Uniaxial Quasistatic and Creep Pro-
    perties of Site Rock," Tech. Mem. Rept. RSI-0029, RE/SPEC, 1975.

39. Wawersik, W. et al., "Preliminary Determination of Mechanical Properties
    on Rock Salt from S.E. New Mexico, Proc. 17th U.S. Symp. on Rock
    Mechanics, Snowbird, Utah, August, p. 5C61-7, 1976.

40. Dropek, R., Pressure-Temperature Creep Testing as Applied to Commercial
    Salt, Master's Thesis (Unpubl) Univ. of Utah, 1976.

SECURITY CLASSIFICATION OF THIS PAGE (When Data Entered)

REPORT DOCUMENTATION PAGE

READ INSTRUCTIONS
BEFORE COMPLETING FORM

1. REPORT NUMBER	2. GOVT ACCESSION NO. AD-A150620	3. RECIPIENT'S CATALOG NUMBER

4. TITLE (and Subtitle)

Geotechnical Assessment of United States and Foreign Test Sites and Material Properties of Geologic Media

5. TYPE OF REPORT & PERIOD COVERED

Final Report

6. PERFORMING ORG. REPORT NUMBER

7. AUTHOR(s)

H. R. Pratt   D. Gardiner
H. S. Swolfs
S. W. Butters

8. CONTRACT OR GRANT NUMBER(s)

Project No ARPA Order 3134-A3
Program Code No 7F10
DNA001-77-C-0122

9. PERFORMING ORGANIZATION NAME AND ADDRESS

Terra Tek, Inc.
420 Wakara Way
Salt Lake City UT 84108

10. PROGRAM ELEMENT, PROJECT, TASK AREA & WORK UNIT NUMBERS

11. CONTROLLING OFFICE NAME AND ADDRESS

Defense Nuclear Agency
Headquarters
Washington DC 20305

12. REPORT DATE

June, 1979

13. NUMBER OF PAGES

14. MONITORING AGENCY NAME & ADDRESS(if different from Controlling Office)

15. SECURITY CLASS. (of this report)

Unclassified

15a. DECLASSIFICATION DOWNGRADING SCHEDULE

16. DISTRIBUTION STATEMENT (of this Report)

17. DISTRIBUTION STATEMENT (of the abstract entered in Block 20, if different from Report)

18. SUPPLEMENTARY NOTES

include:

19. KEY WORDS (Continue on reverse side if necessary and identify by block number)

material property, and salt   stress
triaxial   shale   reduced displacement potential (RDP).
uniaxial   sandstone

20. ABSTRACT (Continue on reverse side if necessary and identify by block number) This report includes a compilation of both physical and mechanical property data for use in developing in situ constitutive relations. The in situ stress state is defined for a variety of rock types and structural environments. Triaxial tests, including hydrostatic and uniaxial strain tests, were conducted on sandstone and shale from the GASBUGGY site. Problems studied include the intact versus residual failure envelopes, dilatant behavior and the dependency of modulus on strain-rate. Salt cores from both the GNOME event and SALMON event were tested under triaxial conditions; both compression and extension failure envelopes were determined. Originator Keywords

DD FORM 1473 EDITION OF 1 NOV 65 IS OBSOLETE
JAN 73